

Materials Design Principles for the Dynamic Fracture of Laminar Composite Structures

Final Progress Report for the Period August 15, 2005 – December 29, 2009
Agreement No. W911NF-05-C-0073

1. Foreword

Crack bridging (e.g., from stitches or pins) and friction have profound and potentially very useful effects on delamination crack growth, controlling growth rates (damage levels) and the energy absorbed. However, the implications for structural design principles have remained quite obscure. The difficulty is that no simple analogue of crack toughness, which underpins static structural design, exists for dynamic cases with large scale bridging effects. The external shape of the structure and the loading configuration dictate stress waves, frictional contact zones, and crack tip stress intensity factors in a way that is very difficult to approach, other than by brute case-specific numerical simulation. The problem is compounded by the common occurrence of multiple cracking, a complexity that is rarely entertained in laboratory fracture specimen design. Physically sound material models for the important structural problem of multiple, nonlinear cracking in laminated structures with large-scale bridging due to friction and reinforcement had previously remained undeveloped, in spite of the technological importance of these systems.

We conducted a program of basic research to develop engineering principles for dealing with dynamic, multiple cracking damage in laminated structures, including large scale crack bridging due to through-thickness reinforcement and friction. Bridging and friction were treated by materials models at the smallest scales relevant to the mechanisms. By reference to the fundamentals of the dynamic growth of single cracks, which is already largely understood, simple approaches have been formulated for calculating the development of distributed delamination cracks in laminated structures. To treat large scale bridging effects, structural sub-component models must support dimensions of ~ 100 mm or more. Our approach therefore bridged scales ranging from this characteristic size down to that of micromechanisms (friction, fiber bridging) within the process zone of a single crack. Thus a direct link has been established between structural performance and materials design.

Our research contributes to a systematic method for simplified design of laminated engineering structures, which will impact the design and performance of all lightweight military vehicles and structures. Newly gained understanding points the way to significant improvements in impact and ballistic resistance via materials and structural design.

The program was conducted with formal collaborations with ARL at Aberdeen, as well as universities in the U.S., Italy, Denmark, and Australia. The university collaborations involved Ph.D. candidate students, who made extended stays at Teledyne Scientific (formerly Rockwell Scientific).

Report Documentation Page			Form Approved OMB No. 0704-0188		
Public reporting burden for the collection of information is estimated to average 1 hour per response, including the time for reviewing instructions, searching existing data sources, gathering and maintaining the data needed, and completing and reviewing the collection of information. Send comments regarding this burden estimate or any other aspect of this collection of information, including suggestions for reducing this burden, to Washington Headquarters Services, Directorate for Information Operations and Reports, 1215 Jefferson Davis Highway, Suite 1204, Arlington VA 22202-4302. Respondents should be aware that notwithstanding any other provision of law, no person shall be subject to a penalty for failing to comply with a collection of information if it does not display a currently valid OMB control number.					
1. REPORT DATE 2009		2. REPORT TYPE		3. DATES COVERED 01-08-2005 to 30-12-2009	
4. TITLE AND SUBTITLE Materials Design Principles for the Dynamic Fracture of Laminar Composite Structures			5a. CONTRACT NUMBER W911NF-05-C-0073		
			5b. GRANT NUMBER		
			5c. PROGRAM ELEMENT NUMBER		
6. AUTHOR(S)			5d. PROJECT NUMBER		
			5e. TASK NUMBER		
			5f. WORK UNIT NUMBER		
7. PERFORMING ORGANIZATION NAME(S) AND ADDRESS(ES) Teledyne Scientific & Imaging, LLC, 1049 Camino Dos Rios, Thousand Oaks, CA, 91360			8. PERFORMING ORGANIZATION REPORT NUMBER ; 48414.5		
9. SPONSORING/MONITORING AGENCY NAME(S) AND ADDRESS(ES) U.S. Army Research Office, P.O. Box 12211, Research Triangle Park, NC, 27709-2211			10. SPONSOR/MONITOR'S ACRONYM(S)		
			11. SPONSOR/MONITOR'S REPORT NUMBER(S) 48414.5		
12. DISTRIBUTION/AVAILABILITY STATEMENT Approved for public release; distribution unlimited					
13. SUPPLEMENTARY NOTES					
14. ABSTRACT					
15. SUBJECT TERMS					
16. SECURITY CLASSIFICATION OF:			17. LIMITATION OF ABSTRACT Same as Report (SAR)	18. NUMBER OF PAGES 48	19a. NAME OF RESPONSIBLE PERSON
a. REPORT unclassified	b. ABSTRACT unclassified	c. THIS PAGE unclassified			

2. Table of Contents

1.	Foreword	1
2.	Table of Contents	2
3.	List of Appendices, Illustrations, and Tables	3
4.	Statement of the Problem Studied	4
5.	Summary of the most Important Results	5
6.	List of all Publications Supoorted under this Contract	7
7.	List of all Participating Personnel	9
8.	Report of Inventions	11
9.	Appendix	12

3. List of Appendices, Illustrations, and Tables

Appendix – preprint of one journal paper:

Lundsgaard-Larsen, C., Massabò, R., and Cox, B.N., On Acquiring Data for Large-Scale Crack Bridging at High Strain Rates, to be submitted to *Engng Fract. Mechanics*.

Illustrations:

none

Tables:

none

4. Statement of the Problem Studied

In this program of basic research we:

- (i) formulated and solved multiple delamination problems by methods that are applicable to reasonably complex structures and loading, and correctly described fundamental aspects of dynamic delamination crack growth in the presence of large scale bridging and friction;
- (ii) provided the fundamental theory necessary to establish engineering principles for modeling and designing laminated structures with energy absorption optimized by tailoring crack bridging and friction mechanisms.

The main thrust of our work was theoretical. Use was planned to be made of new data anticipated from a separately funded dynamic fracture study to be conducted at Purdue University. Unfortunately, substantial delays in specimen preparation have resulted in these data still being unavailable, which prevented us from completing a quantitative study of engineering design principles for pinned laminates, our original goal. Nevertheless, while such work cannot be included in this report, the experiments are still proceeding and the principal investigators of this project (Dr. Brian Cox with consultative support from Dr. Roberta Massabò) are personally committed to analyzing the data when they are available (see below).

Our objectives were to:

Conduct basic research into the development of distributed dynamic delamination cracks in laminated structures with non-trivial geometry and general loading conditions and in the presence of friction and bridging due to through-thickness reinforcement such as stitches or rods.

Develop engineering principles for dynamic, multiple cracking in laminated structures, including large scale crack bridging and friction.

Create a systematic method for simplified design of laminated engineering structures containing through-thickness reinforcement, which will shorten the design cycle for lightweight military vehicles and structures.

Indicate means for achieving significant improvements in impact and ballistic resistance via materials and structural design, especially via manipulation of friction or the bridging effects of through-thickness reinforcement.

5. Summary of the Most Important Results

Our research addressed the objectives by pursuing the following research themes. Numbered references refer to the publication list in Section 6.

(i) We contributed to the development of virtual tests for composite materials, which is to say simulations of such high fidelity that they can be substituted for most (but not all) of the experiments currently needed to achieve an optimal design [3,5]. The Virtual Test paradigm offers a framework for implementing the type of model we developed in this program in a materials design tool for dynamic applications. We also organized a minisymposium on Virtual Tests at the International Conference on Computational Mechanics in Italy in 2008, which is one of the largest and most important global conferences in the field. An edited special issue of the *International Journal of Fracture* [8].

(ii) We modeled the problem of dynamic pullout of a through-thickness bridging entity, showing that inertial effects tend to stiffen the pullout response in velocity regimes expected in engineering applications [2]. The stiffening, as a rule of thumb, is of order of magnitude a factor of two. The dynamic solutions to the pullout problem possess some complex and interesting characteristics.

(iii) As part of the process of developing engineering design rules for through-thickness reinforcement, we made a collation of published data on the properties of pinned, stitched, and woven laminates [12]. Interpretations of trends in data were made based on existing micromechanical models, many of which we have developed in our group. This practically motivated exercise reveals very clearly what properties can be manipulated effectively by reinforcement design and what properties are subject to variance that is so severe that no useful design principle can be confirmed. The collation also highlights shortcomings in the manner in which data are presented, especially the lack of necessary detail concerning the materials studied. One conclusion of the paper is that trends in delamination failure are reasonably well predicted by micromechanical models that describe the bridging effects of pins and stitches in static loading, provided data on the subject materials are sufficiently complete and carefully [12]. In a related study on pinned laminates, we successfully accounted for rate effects at high temperature with an elaboration of analytical models of pin mechanics [6]. This encourages similar analysis of inertial effects in mixed mode loading.

(iv) As part of our preparation for modeling multiple delaminations in beams, we revisited the fundamental problem of how to calculate the energy release rate for a delamination crack accurately using modified beam theory [4]. The results of this work have since been confirmed in computational work (finite element methods) by one of our colleagues, who reports that they are extraordinarily accurate and significantly more accurate than previous modified beam theories (Dr. Qingda Yang, University of Miami, private communication).

(v) We then proceeded with a series of theoretical analyses of the mechanics of dynamic delamination cracks. Key phenomena studied, in both static and dynamic conditions, include the shielding and acceleration of one crack by a neighboring crack, and the stability of equality of length of a system of simultaneously propagating cracks

[1,7,9-11]. These characteristics control the qualitative behavior of multi-delamination systems and therefore control damage tolerance and energy absorption.

(vi) Seeking to couple our theories to experimental observations and test data, we undertook a joint program of experiment and theory to determine rate dependence in the crack bridging behavior of through-thickness reinforcement under dynamic loading. We seek general materials design data by which optimal damage control and ballistic performance can be achieved by intelligent exploitation of stitching and z-pinning in composite structures. In this effort, we carried out detailed theoretical analyses of the dynamic delamination behavior expected in tests to be carried out at Purdue University (Dr. Wayne Chen). The analyses bear out just how complicating dynamic effects can be to the delamination problem [9-11]. Nevertheless, examination of certain limiting conditions that hold in part of the solution space allows very useful conclusions to be drawn about the best test conditions for inferring the required dynamic constitutive behavior of through-thickness reinforcement [11]. The key paper in this study is complete but not yet published [11]. We therefore include it here as an appendix. A highly simplified summary of desirable test conditions has been sent to Purdue [13]. The tests are expected to be executed in the next few months and Drs. Massabò and Cox have agreed to analyze the data without funding. Analysis should be complete towards the end of 2010.

The Purdue test program was delayed for two years by difficulty with materials processing. Specimens that were finally delivered from ARL to Dr. Chen were of poor quality, containing substantial porosity (unconsolidated material). The supplier for ARL was apparently unable to overcome these deficiencies. Therefore, we arranged for our long-term collaborator Dr. Adrian Mouritz of RMIT University, Melbourne, Australia, to fabricate specimens gratis for this test program. The specimens from Dr. Mouritz were delivered to Dr. Chen in the summer of 2009 and one of Dr. Chen's students is testing them in 2010.

As our publication list shows, all aspects of this program were conducted in a collaborative manner within a global network of university and other researchers. The most important collaboration was with Professor Roberta Massabò of the University of Genova, Italy, who was supported by a small subcontract under this program. A number of graduate students were involved in our work.

6. List of all Publications Supported under this Contract

(a) Papers published in peer-reviewed journals

1. Andrews, M.G., Massabò, R., Cox, B.N., 2006. Elastic interaction of multiple delaminations in plates subject to cylindrical bending. *International Journal of Solids and Structures* **43**, 855-886
2. Yang, Q.D., Rosakis, A.J., Cox, B.N., 2006. Dynamic fiber sliding along debonded, frictional interfaces. *Proceedings of the Royal Society A* **462**, 1081-1106.
3. Cox, B.N., Yang, Q.D., 2006. In quest of virtual tests for structural composites. *Science* **314**, 1102-1107.
4. Andrews, M.G., Massabò, R., 2007. The effect of shear and near-tip deformations on energy release rate and mode mixity of edge-cracked orthotropic layers. *Engineering Fracture Mechanics*, **74**, 2700-2720.
5. B. N. Cox, S. M. Spearing, and D. R. Mumm, "Practical challenges in formulating virtual tests for structural composites," chapter in *Mechanical Response of Composites*, ed. P. P. Camanho, C. G. Dávila, S. T. Pinho, J. C. C. Remmers, Springer Science and Business Media, Dordrecht, 2008.
6. P. Chang, A. P. Mouritz, and B. N. Cox, "Elevated temperature properties of pinned composite lap joints," *Journal of Composite Materials*, **42**[8], 741-69 (2008)
7. M. G. Andrews, R. Massabò, A. Cavicchi, and B. N. Cox, "Dynamic interaction effects of multiple delaminations in plates subject to cylindrical bending," *Int. J. Solids and Structures*, **46**, 1815-1833 (2009)
8. Edited volume: J. Llorca and B. N. Cox (eds.), "Virtual Tests for Composite Materials," Proceedings from the World Congress on Computational Mechanics, Venice, July, 2008, special volume in *International Journal of Fracture*, in press (2009).

(b) Papers published in non-peer-reviewed journals or conference proceedings

9. C. Lundsgaard-Larsen, R. Massabò, and B. N. Cox, "Designing dynamic tests to assess rate dependence in large-scale crack bridging," in *Proceedings, Int. Conf. on Composite Materials ICCM-17*, Edinburgh, July, 2009, ed. M. Wisnom
10. C. Lundsgaard-Larsen, R. Massabò, and B. N. Cox, "The design of dynamic tests to infer rate dependence in large-scale crack bridging," in *Proceedings, Int. Conf. of the Society for Experimental Mechanics, SEM*, Albuquerque, NM, June 2009, pp. 1-10

(c) Papers presented at meetings but not published

none

(d) Manuscripts submitted, not published

11. Lundsgaard-Larsen, C., Massabò, R. and Cox, B.N., On Acquiring Data for Large-Scale Crack Bridging at High Strain Rates, to be submitted to *Engng Fract. Mechanics*.
12. A. P. Mouritz and B. N. Cox, "A mechanistic interpretation of the comparative in-plane mechanical properties of 3D woven, stitched and pinned composites," *Composites Part A*, in press.

(e) Technical reports submitted to ARO

13. Cox, B.N., Massabò, R., and Lundsgaard-Larsen, C., Report on Test And Material Specifications For Dynamic Delamination Studies Of Z-Pinned Laminates, August, 2007.

(f) Ph.D. Thesis

7. List of all Participating Personnel

The following people have been directly supported by the ARO grant at some period of our contract support. Some of them continue to collaborate after moving on to new positions, under other funding.

Dr. Qingda Yang, Member of Technical Staff, Rockwell Scientific Co. LLC (now at the University of Miami)

Dr. Brian Cox, Principal Scientist, Teledyne Scientific Co. LLC and Adjunct Professor, Sydney University, Sydney, Australia

Professor Roberta Massabò, University of Genova, Genova, Italy and Adjunct Professor, Northwestern University, Chicago, Illinois

Dr. Martin Andrews, Ph. D. candidate and Postdoctoral Fellow, Northwestern University and University of Genova, Genova, Italy (supervisor, Professor Roberta Massabò).*

Dr. Andrea Cavicchi, Postdoctoral Fellow, University of Genova, Genova, Italy (supervisor, Professor Roberta Massabò).

Mr. Weixing Josh Zhou, Ph. D. candidate, University of Illinois at Urbana Champaign (supervisor, Professor Yonggang Young Huang).**

Mr. Christian Lundsgaard-Larsen, Ph. D. candidate, Technical University of Denmark, Lyngby, Denmark.***

A new graduate student at the University of Genova, who will use the code developed by Mr. Lundsgaard-Larsen to analyze dynamic fracture tests.

Ms. Holly Barth, University of California, Berkeley; Ph. D. candidate.

*Dr. Andrews earned a Ph. D. (Northwestern University) partly while supported by this contract.

**Mr. Zhou visited Teledyne Scientific (Rockwell Scientific at the time) as part of his thesis work for a six-month assignment in our Thousand Oaks facility under the supervision of Drs. Qingda Yang and Brian Cox, beginning January 1, 2006.

**Mr. Lundsgaard-Larsen visited Teledyne Scientific as part of his thesis work to work for six months in our Thousand Oaks facility under the supervision of Dr. Brian Cox beginning in September, 2006. After this, he and his supervisors, Dr.s Jorgen Jensen, Christian Berggreen, and Bent Sorenson, have continued a collaboration on delamination mechanics.

Further collaborative work – a global network for Virtual Tests

The following three collaborations involve no ARO funding, except to a limited extent to enable the participation of Brian Cox at Teledyne Scientific.

- A proposal has been written (without charge to ARO) to the Australian Research Grants Council with Professor Adrian Mouritz at the RMIT University, Melbourne, to fund basic research into through-thickness reinforcement.
- A project under Professor Mark Spearing, University of Southampton, continues under funding from the UK EPSRC. Professor Spearing collaborates on delamination damage detection experiments using micro-CT to create 3D images of damage.
- A new agreement involving no funding has been reached with the group of Dr. Howard Padmore at the Advanced Light Source at LBL and Professor Rob Ritchie, UC Berkeley, to study damage in composites using x-ray computed tomography. Professor Ritchie has made a Ph. D. student, Ms. Holly, available for this work.

While these collaborative projects brought no funding to Teledyne Scientific, they enabled collaborative work involving further students at RMIT University, Southampton University, and UC Berkeley with technical exchange facilitated by visits.

- We continue work on a program awarded by NASA for calibrating cohesive laws for delamination propagation in laminated composites containing no through-thickness reinforcement. This work focuses on studies in the non-dynamic regime, but formed a useful background to our dynamic fracture studies.

All of these collaborations and other contracts contributed to our vision of constructing a virtual test for composites.

8. Report of Inventions

There have been no inventions in this contract to date.

9. Appendix

Lundsgaard-Larsen, C., Massabò, R. and Cox, B.N., On Acquiring Data for Large-Scale Crack Bridging at High Strain Rates, to be submitted to *Engng Fract. Mechanics*.

On acquiring data for large-scale crack bridging at high strain rates

C. Lundsgaard-Larsen¹, R. Massabò² and B.N. Cox³

¹Technical University of Denmark, Lyngby, Denmark

²DICAT, University of Genova, Genova, Italy

³Teledyne Scientific Co LLC, Thousand Oaks, CA, U.S.A

Abstract. Numerical simulations are used to design test geometries and loading histories that are suitable for probing the mode II bridging effect of through-thickness reinforcement at high strain rates. The bridging effects are represented by a cohesive law and tests are sought that will determine any rate dependence in its parameters. The End Notched Flexural test is studied, because it allows easy application of time dependent loading and has proven to be an information-rich test in the quasi-static case. Information content in the dynamic case is addressed by focusing on regimes within the full computed solution space where crack growth is approximately steady-state. This condition simplifies the inverse procedure for identifying model parameters, clarifying the prospective information content of experiments. Numerical results show that hypothetical rate-dependence in the cohesive law causes strong and measurable changes in the regime of steady-state behavior, if the tests are properly selected to vary the crack sliding speed. The estimates of information content are conservative, in that analysis of the total solution space will necessarily contain more information than analysis of the steady-state regime alone.

Keywords: Dynamic Delamination Fracture, End Notched Flexural Test, Dynamic Cohesive Law, Computational Modelling, Through-Thickness Reinforcement, Crack Bridging, Parameter Identification

1. Introduction

Through-thickness reinforcement such as stitches or pins can increase the delamination resistance of laminated polymer or ceramic matrix composites by an order of magnitude or more (Cox et al., 1996; Glaessgen et al., 1999; Holt, 1982; Lee and Liu, 1990; Mouritz and Cox, 2000; Rhodes and Williams, 1981; Sawyer, 1985; Tada and Ishikawa, 1989; Turettini, 1996). The load required to propagate a delamination crack across fracture specimens can be raised by through-thickness reinforcement, which extends the pre-critical domain that precedes unstable crack growth, thus improving ductility and damage tolerance. These trends offer the materials designer significant opportunities for matching the performance of a material to specific applications, especially where damage tolerance and energy absorption are strongly desired. However, potential benefits can be pre-empted by adverse effects of the reinforcement on other failure mechanisms (Mouritz and Cox, 2000). Therefore, careful selection of the parameters of the through-thickness reinforcement is needed, which must be based on experimental characterization of the performance of through-thickness reinforcement in relevant dynamic regimes. The non-trivial question of how to acquire such data is the subject of this paper.

An expanding body of test data has now been published on the crack bridging effects of stitches and pins under static loading, both for single stitches or pins in model specimens and for arrays of stitches or pins bridging cracks in delamination specimens (Cartié et al., 2004; Chang et al., 2006; Cox, 2005; Dransfield et al., 1994; Dransfield et al., 1998; Jain and Mai, 1995; Jain et al., 1998; Massabò et al., 1998; Mouritz and Cox, 2000; Rugg et al., 1998; Sun et al., 2004; Tong et al., 1998a; Tong et al.,

1998b; Turettini, 1996). The observed mechanisms of deformation of the reinforcement under mixed mode loading have been modeled with reasonable success, so that a good understanding exists of the main material factors influencing the efficacy of pins or stitches as bridging entities (Chang et al., 2008; Cox, 2005; Cox and Sridhar, 2002). The bridging effect can be represented accurately by a cohesive traction law in a nonlinear fracture model. Accurate accounts of static delamination test data can be obtained by inserting the traction law into fracture simulations.

As well as its benefits in static loading, through-thickness reinforcement has also been shown to successfully counteract negative effects in dynamic delamination fracture and macrostructural behavior that arise from the inertia of the specimen and dynamic vibrations (Andrews et al., 2009; Brandinelli and Massabò, 2003). However, this and other theoretical studies assume that the constitutive behaviour of the through-thickness reinforcement is approximately the same under dynamic conditions as it is under static conditions. This may not be the case. In fact, some indications already exist that rate effects should be expected in the traction laws that represent bridging due to through-thickness reinforcement. Experiments in which fibres were pulled out of a substrate at rates of 1 mm/min and 100 mm/min show that the friction between the pulled out fibres and the laminate increases with speed (Liu et al., 2007). A possible physical explanation given by the authors is visco-elastic behaviour of the fibre/matrix interface, coupled with a temperature increase due to friction. Theoretical studies of the micromechanics of fiber pullout also show that the inertia of the fibers will create rate effects in the fibre pull-out problem (Cox et al., 2001; Sridhar et al., 2003).

No research has been reported in which the bridging tractions have been deduced from fracture tests in the dynamic regime, where the inertia or dynamic material properties might change the bridging effect. This lack can frustrate optimal design, because optimality does not necessarily result from inserting the maximum through-thickness reinforcement density. While some properties rise monotonically as the density increases, cost, in-plane properties, and energy absorption can all be affected unfavorably. Through-thickness reinforcement is expensive and causes harm to in-plane fibers, compromising strength and fatigue life. If the through-thickness reinforcement is too effective in suppressing delamination, it can cause the structure to exhibit brittle failure characteristics, with minimal energy absorption, a disadvantage for ballistic performance. The quest for optimality can therefore be subtle and demands quantitative knowledge of the effects of the through-thickness reinforcement. Furthermore, to acquire all of this knowledge by repeated cycles of fabricating and testing structures with different material compositions is prohibitively expensive.

The question therefore arises of what experiments will be most useful for acquiring data that determine the high strain rate behavior of through-thickness reinforcement. The desired information-rich experiment should:

- generate dynamic crack propagation in the range of speeds where the effects of through-thickness reinforcement will be strongest, in particular avoiding large crack speeds for which the process is dominated by the kinetic energy and the effects of the reinforcement become negligible (Sridhar et al., 2002);
- generate crack propagation in the domain where the process zone is developing and also where it is fully developed, thus maximizing the information content pertaining to all model parameters;
- avoid large flexural oscillations of the specimen as well as the development of high order, high frequency waves in the desired range of crack speeds;
- avoid the formation of multiple cracks in the specimen;
- avoid failure by mechanisms other than delamination fracture.

Numerical studies are used in this paper to find such experiments. A simplified procedure is proposed that allows quick insight into the information content of candidate dynamic fracture experiments.

2. Choice of specimen geometry and material properties

The subject specimen is an ENF specimen loaded in three-point bending, see Figure 1. Choosing an ENF configuration for this pilot study avoids the complexity of mixed mode crack conditions and allows relation to the well-studied static case of mode II fracture in the presence of large scale bridging (Massabò et al., 1998; Massabò and Cox, 1999; Brandinelli and Massabò, 2006).

The length scales that control nonlinear fracture in delamination beams (slender bodies) under quasi static pure mode II loading are well understood (Suo et al., 1992; Massabò and Cox, 1999). The small scale bridging length scale, l_{SSB} , defines the length of the process zone of a crack propagating under small scale bridging conditions, where the length of the process zone is constant and much smaller than the crack length and all other relevant lengths of the problem, and the crack propagates with a constant fracture energy. Consider a rectangular cohesive law, with σ_0 the cohesive tractions, δ_c the critical crack displacement, and $G_b = \sigma_0 \delta_c$ the cohesive fracture energy. The quasi-static small scale bridging length is given by:

$$l_{SSB} = \sqrt{a_{IIs} h} \quad (1)$$

$$a_{IIs} = \delta_c \bar{E} / (4\sigma_0)$$

where $\bar{E} = E / (1 - \nu_{zx} \nu_{xz})$ with E the longitudinal Young's modulus and ν_{ij} Poisson coefficient. In thin bodies, the lengths of process zones scale with the thickness of the body h . A mode II delamination crack approaches the characteristic length from above as it propagates: the process zone length increases from zero at crack initiation to some value that is larger than the small scale bridging limit and depends on the geometry and loading conditions, and then tends to the small scale bridging limiting value.

The formula in Eq. (1) is accurate length when the applied load can be represented by uniform shear tractions acting along the crack faces, the case for $a < L$ in an ENF specimen. For more complex loads, including the ENF specimen with $a \geq L$, variations can be expected in the process zone length. Variations in l_{SSB} of order unity will also arise when the shape of the cohesive law departs from the rectangular law used in deriving Eq. (1) (Massabò and Cox, 1999), e.g., the triangular laws used in this paper (Smith, 1989; Bao and Suo, 1992). Finally, Eq. (1) was derived for quasi static loading conditions. Dynamic conditions introduce further variations in the zone length. For example, the zone length in steady state propagation decreases monotonically with crack tip speed (Freund, 1989). However, provided the crack tip speed is modest, e.g., $v_{tip} < 0.2c_R$, with c_R the Rayleigh wave speed, variations are less than 5%. Moderate velocities are of most interest for studying crack bridging, because at higher speeds the kinetic energy of the fracturing material dominates crack propagation and bridging has no useful effect (Sridhar et al, 2002). Thus Eq. (1) is only an approximate indicator of the zone length in small scale bridging conditions, but is still useful in understanding trends in fracture.

The ACK length scale (after Aveston, Cooper, and Kelly, Aveston et al., 1971), l_{ACK} , gives an order of magnitude indication of the distance a crack must propagate to approach the ACK limit, where bridging ligaments remain intact, so that the crack propagates noncatastrophically with a constant critical value

of the applied load. The ACK length scale is given by $l_{ACK} = \sqrt{a_{lim} h}$, where $a_{lim} = E\delta_c / 4\sigma_0$ for a linearly increasing bridging traction law (Massabò and Cox, 1999).

Specimen dimensions (Fig. 1) were chosen in the simulations to take account of the anticipated length scales, and also some other considerations. The specimen length should be longer than the process zone length at all times to accommodate steady-state propagation of a mature zone. However, if the specimen becomes very long this will lead to awkwardly large deflections. Simulations show that if the loading displacement is applied at a high acceleration at the midpoint of a very long slender specimen, the material close to the load point will move much faster than the material distant from the load point, which is constrained by inertia. This leads to a deflection shape remarkably different from the quasi-static case, and this non-equilibrium state will eventually lead to oscillatory behaviour of the specimen. This effect, which is also present in an initial transient phase in short specimens, becomes predominant when the specimen length is increased, which is the reason for choosing a relatively short specimen of a length (between supports) of $2L = 100$ mm (Fig. 1). For specimen thickness, a thicker arm reduces the maximum normal stresses at the upper and lower surfaces of the specimen, but increases the size of the process zone (Eq. 1). For the chosen thickness of $2h = 10$ mm the maximum stresses in the longitudinal direction of the beam subject to quasi-static loading are well below the tensile and compressive strengths of the assumed material (Table 1). This should ensure avoidance of failures at the upper or lower surfaces of the beam in the dynamic tests. Finally, the pre-crack length should be long enough to avoid unstable crack growth, yet short enough for the process zone to develop and reach a certain speed before the crack tip reaches the end of the specimen. Based on numerical analysis for representative large scale bridging the notch length is chosen to be 20 mm, i.e. $a_0 = 0.4L$.

The material is assumed to be linear elastic with material properties typical of carbon fibre reinforced epoxy. Properties correspond to an in-plane quasi-isotropic lay-up as listed in Table 1.

3. Finite element model

The 2-D finite element model consists of two layers connected through zero thickness cohesive elements that partly cover the beam length (Fig. 2). The pre-crack consists of the part of the beam without cohesive elements. A frictionless contact interaction is formulated in a penalty master-slave configuration between the two layers to prevent interpenetration. The mesh in the layers is uniform with a refinement near the interface with a ratio of four between the side length of the smallest and largest elements. Nodes between bulk and cohesive elements are coincident and the side length of the cohesive elements is $0.0025L$; this length satisfies the requirement that the cohesive zone should span several cohesive elements at all times during the simulations. Mesh convergence is found by varying the element size.

Three idealised cohesive laws are considered, one representing a laminate without through-thickness reinforcement (triangular) and two representing laminates with through-thickness reinforcement (triangular and trapezoidal). The properties of the cohesive laws are illustrated in Fig. 3 and listed in Table 2. The shapes of the laws and the parameter values in Table 2 are approximately consistent with those expected for z-pins or reinforcing rods or continuous stitches that fail and pull out of the laminate (Cartié et al., 2004; Cox, 2005; Turettini, 1996). The cohesive laws with an area below the traction-separation curve of $G_b = 5.0 \text{ kJ/m}^2$ and critical displacement $\delta_c = 0.5 \text{ mm}$ correspond to laminates with through-thickness reinforcement, whereas the area and critical displacement for laminates with no through-thickness reinforcement are reduced by a factor of 10 from the triangular case with through-thickness reinforcement, which is an estimate based on previous experience. The initial linear branch of

the cohesive laws is chosen to be very stiff to limit the influence of the cohesive elements in the intact portion of the beam on the overall compliance of the specimen: the displacement δ_0 at the end of the initial branch is then chosen to be 1.7 and 3.3 microns for the trapezoidal and triangular-shaped cohesive laws, respectively. For the simulations performed in the last section of the paper and the derivation of behavioral maps, additional values have been used for the parameters σ_0 , δ_0 and δ_c .

In a cohesive interface model there is no crack tip singularity. The position of the crack tip, or leading edge of the process zone, is identified as the point where damage starts, namely the point where the cohesive element displacement equals δ_0 and the cohesive traction-displacement relation deviates from the initial linear regime. The trailing edge of the process zone is the point where the cohesive element displacement equals δ_c (Fig. 3).

The model is implemented in the commercial finite element code ABAQUS 6.6, which solves the problem in the explicit domain and includes inertia effects. The 4-node plane strain element CPE4R and 4-node element COH2D4 are used for the layers and the interface, respectively. The density of the interface elements is chosen so that the total mass of the interface is 1/10 of the total mass, which is small enough not to add extra mass to the system and large enough to limit any effects on the automatically calculated time step. The implementation of the cohesive laws in ABAQUS is based on the damage model proposed by Camanho et al. (2003), which defines the mode I and mode II cohesive tractions as functions of a single damage variable (coupled model). Since mode I displacements at the interface are always very small in all cases examined, the model is essentially equivalent to a classical uncoupled cohesive zone model.

4. Loading history

In the simulations the specimen is loaded in displacement control. The loading history is an idealisation of experimental loading conditions similar to those of a split Hopkinson pressure bar with a special pulse shaper (Song and Chen, 2004). The velocity of the load point is zero at time $t = 0$ and increases linearly to a constant speed v_0 over the time t_0 (Fig. 4). If v_0 is small and t_0 large, the loading situation is quasi-static. If the velocity is large and t_0 approaches zero, the loading corresponds to a hard impact and the acceleration in the time interval 0 to t_0 becomes large.

The ramp time t_0 has a large influence on the dynamic fracture behaviour of the specimen. If the ramp time is short, high frequency vibration modes may be excited, leading to an oscillating stress state near the crack tip. If the ramp time is large, crack propagation may occur before the applied loading speed has reached the final value and large values of crack tip speeds and sliding speeds may not be reached. The challenge is to choose a ramp time sufficiently small to obtain rapid crack growth, yet sufficiently large to avoid a highly fluctuating fracture behaviour. Andrews et al. (2009) analysed the effect of ramp time on the dynamic amplification of the energy release rate for specimens with a stationary crack subject to a step force with a finite rise time. They found that if the ramp time was equal to the first natural vibration period T_1 , there was no dynamic amplification, and no subsequent oscillations. Conversely, smaller rise times led to oscillations in the specimen. The cases studied in Andrews et al. (2009) differ from the present, since loading was force controlled and the crack was stationary. However, by considering the fracture behaviour of the tested specimens at various ramp times, the choices $t_0 = T_1$ and $t_0 = T_1/2$ were found to be suitable compromises to obtain rapid crack growth while limiting stress wave effects.

The first natural vibration period T_1 was defined through an eigenvalue analysis of the specimen. During the analysis the specimen is supported at the three points where it is loaded by the test machine in three-point bending (Fig. 1). The bond-line outside the pre-crack is assumed intact and the nodes between the two beams are fixed except along the pre-crack where linear elastic cohesive elements are inserted. The cohesive elements are given a very large stiffness in the normal direction and a negligible stiffness for tangential deformation to allow sliding but restrain normal opening of the pre-crack (constrained vibration model). This ensures that only the relevant natural vibration modes will appear in the analysis, i.e., normal opening of the pre-crack is prohibited, and that the problem remains linear (contact between crack surfaces is avoided). For a specimen of length $2L = 100$ mm the oscillation period is $T_1 = 188$ μ s. Therefore, ramp times $t_0 = 188$ and 94 μ s were chosen for subsequent analyses. For a longer specimen of length $2L = 210$ mm, $T_1 = 588$ μ s, and thus $t_0 = 588$ μ s was chosen for the simulations of long specimens described below.

5. Results for Quasi-static Loading

It is beneficial first to consider the results from quasi-static loading to distinguish between static and dynamic effects. In the quasi-static analyses in this study a loading rate $v_0 = d\Delta/dt = 0.05$ m/s is found to be sufficiently slow, convergence analysis showing no visible dynamic effects.

5.1 Laminate without through-thickness reinforcement

In Figure 5, the reaction force vs. applied displacement, and the positions of the leading and trailing edge of the crack vs. applied displacement, are plotted for quasi-static loading of a specimen with no through-thickness reinforcement ($G_b = 0.5$ kJ/m² and $t_0 = T_1$). Initially, the force increases linearly up to a load point displacement of 0.2 mm, at which point the leading edge starts to propagate. Propagation is stable up to an applied displacement of 0.55 mm. Thereafter, the leading edge of the crack propagates unstably, which entails a sudden drop in the applied load and small oscillations in the reaction force history; simultaneously, the trailing edge of the crack starts to propagate. The dashed line in subplot a) represents the calculated load-displacement relation of the fully cracked specimen. This is calculated from shear deformable beam theory by assuming two centre loaded, simply supported beams each of thickness h . As expected, the load-displacement relation approaches this line as the crack length increases to span the whole length of the specimen.

The process zone length (found as the distance between the leading and trailing edges of the process zone, i.e. the vertical distance between curves in Figure 5b) is shown in Fig. 6 as a function of load point displacement. A maximum process zone length of 13.5 mm is reached just before the unstable crack growth occurs. The zone length decreases monotonically throughout the remaining part of the simulation. The estimate of the small scale bridging limit is $l_{SSB} = \sqrt{\delta_c \bar{E} h / (4\sigma_0)} = 13$ mm, Eq. (1). The curve in Fig. 6 tends to a smaller horizontal asymptote. This is due to the fact that a triangular cohesive law has been used and the concentrated reaction force at the mid-span generates non-uniform stress and displacement fields at the bond line when $a \geq L$, whereas Eq. (1) was derived for a rectangular law assuming uniform fields.

5.2 Laminate with through-thickness reinforcement

Results for the cases representing laminates with through-thickness reinforcement are shown in Fig. 7. Dashed lines represent the trapezoidal cohesive law, whereas solid lines represent the triangular. By considering the reaction force in subplot a) one sees that, in contrast to the case without through-

thickness reinforcement, unstable crack growth does not occur, due to the stabilizing effects of a large process zone. This behavior confirms experimental observations on through-thickness reinforced laminates in (Massabò et al., 1998). Consider the crack length diagram in subplot b): in the specimen with a triangular cohesive law (solid line), the crack tip (leading edge) extends from the pre-crack at a loading displacement of 0.2 mm and the process zone subsequently builds up. As the crack tip passes the centre of the specimen (i.e., the load point corresponding to 50 mm on the vertical axis), the curve suddenly changes slope, and from here the crack tip moves at a monotonically decreasing rate relative to the load point displacement. The process zone size vs. load point displacement is plotted as the solid line in Figure 8. The history of the zone length is qualitatively similar to the non-reinforced case plotted in Fig. 6, except that the zone is much longer (in this case the small scale bridging length scale of Eq. (1) is 41 mm).

The specimen with a trapezoidal cohesive law, which is represented by dashed lines in Figs. 7 and 8, has a different behaviour. Since the critical stress σ_0 is only half that for the triangular law, the process zone develops at a smaller load and the specimen is more compliant during the first 2 mm of loading displacement, see subplot a). In subplot b), the crack tip apparently instantly changes position from 60 mm to 100 mm at a loading displacement of 3 mm. This is a consequence of the formation of a second process zone at the right end side of the specimen when the applied displacement is larger than 1.2 mm. The shear stress distribution along the bond-line of an ENF specimen (when ignoring the stress concentration due to the notch and edge effects) is constant with a change of sign at the midpoint where the load is applied. A process zone may start at a distance from the pre-notch if the shear stress in the intact ligament exceeds the critical stress σ_0 . This occurs in the case of the trapezoidal law. Figure 9a shows the stresses in the normal and tangential directions along the cohesive elements in the intact ligament of the specimen for an applied displacement of 1.2 mm. In the left part of the specimen ($z < 50$ mm), the process zone has developed from the pre-crack for both cohesive laws, since stresses have reached the critical values $\sigma_0 = 20$ MPa and $\sigma_0 = 10$ MPa, respectively. In the right half ($z > 50$ mm), the specimen is undamaged, but the specimen with the trapezoidal law (dashed line) is close to initiating a second process zone, since the shear stress σ_{zy} is approaching -10 MPa. In subplot b), the corresponding opening and sliding displacements are shown. A sliding displacement between 0.003 and 0.5 mm, i.e., between critical displacements δ_0 and δ_c of the cohesive law, indicates that the corresponding cohesive element is inside the process zone.

In Figure 9c the stress distribution in the cohesive elements is plotted at a loading displacement of 3 mm. In the trapezoidal case (dashed line) two separate process zones have developed, the first being the crack that has initiated from the notch and the second being a crack that initiates at the far end of the specimen and propagates back towards the first crack. These two cracks completely cover the left and right part of the specimen, where the stresses are constant and equal to +10 or -10 MPa (the critical traction value of the trapezoidal cohesive law). The load situation shown is the limiting case just before the two process zones join, which occurs as the sliding displacement of the pre-crack tip exceeds the critical displacement $\delta_c = 0.05$ mm, see subplot b) at $z = 20$ mm. The described stress and displacement distribution in the cohesive elements along the bond line at load point displacements of 1.2 and 3.0 mm, respectively, can be compared to the reaction-force and crack length plots in Figure 7. As the two process zones join at an applied displacement of 3.0 mm, the apparent crack tip instantly moves from 60 mm to 100 mm.

The history of the process zone length in Fig. 8 (dashed curve) is influenced by the formation and growth of multiple process zones at applied displacements larger than 1.2 mm. The zone length shows a plateau at around 40 mm, which is well below the small scale bridging length of Eq. (1), $l_{SSB} = 58$ mm for the trapezoidal law.

In summary, when the geometry and cohesive laws parameters are such that the small scale bridging length is comparable to the half length of the specimen and the cohesive law is either trapezoidal or an increasing function of the relative sliding displacement multiple process zones may develop. The risk of this phenomenon, whose presence would complicate the inference of bridging laws, may be reduced by increasing the length of the specimen or reducing its thickness, as shown in the following section.

5.3 Effect of increasing specimen length

When the small scale bridging length is comparable to the half length of the ENF specimen, as in the case of a trapezoidal cohesive law and $2L = 100$ mm, two independent process zones may develop during loading. Simulations for the quasi-static loading case suggest that this will not occur under dynamic conditions if the specimen is made significantly longer. If the specimen length L and the pre-crack length a_0 are increased while a fixed ratio L/a_0 is maintained, the crack propagates at a smaller load. Since the nominal shear stress is proportional to the force applied to the loading point, the shear stress in the intact ligament distant from the pre-crack will not exceed the critical stress σ_0 before the crack has propagated throughout the specimen. Results for specimens with through-thickness reinforcement and length $2L = 210$ mm are plotted in Figure 10. In this specimen, the process zone lengths rise well above the small scale bridging limit for both cohesive laws when the crack is propagating in the first half of the specimen (approaching 60 mm and 72 mm for the triangular and trapezoidal laws respectively). They then decrease while the crack propagates in the second half to 32 mm and 40 mm respectively. The process zone length for the trapezoidal cohesive law is smaller than the small scale bridging value of Eq. 1, 58 mm, at the end of the simulation. This is due to nonuniformity in the stress and displacement fields, as remarked above.

6. Results for High-speed Loading

In the following, results are presented for specimens with and without through-thickness reinforcement, with trapezoidal and triangular cohesive laws, loaded at high speed. A simple method is suggested for relating the process zone sliding speed to the crack tip speed and displacement profile.

6.0 Laminates without Through-Thickness Reinforcement Loaded at High Speed

Figures 11 and 12 refer to a specimen without through-thickness reinforcement, a load point velocity $v_0 = 20$ m/s and a ramp time $t_0 = T_1/2$. Comparison with the quasi-static case in Figure 5 reveals dynamic effects. For the reaction force (Fig. 11a), dynamic effects consist of amplifications and oscillations; the process zone length (Fig. 12) builds up to a much larger value (27 mm) than in the quasi-static case (13 mm) but then quickly approaches an approximately constant value of 8.5 mm (the small scale bridging length of Eq. (1) is 13 mm). In the crack propagation history (Fig. 11b), dynamic effects induce an interval, between 1 mm and 1.2 mm, where the crack tip speeds remain constant and equal to 1015 m/s, which is approximately 20% of the longitudinal wave speed of the material. In this interval, the crack profile remains approximately constant and crack propagation is approximately under steady-state conditions (this will be elaborated in Section 6.2). Similar intervals appear for other

loading rates between 5 and 30 m/s. It will be shown below that steady-state crack propagation domains can give important information about possible rate dependence in the cohesive law. For loading rates above a certain velocity (equal to 30 m/s for this geometry, cohesive law and loading ramp time), multiple process zones may develop along with increased oscillations, which would make experimental results more difficult to interpret.

6.1 Laminates with through-thickness reinforcement loaded at high speed

Figure 13 shows results for a specimen with through-thickness reinforcement for load point velocity $v_0 = 20$ m/s and ramp time $t_0 = T_1$. Comparison with the quasi-static case in Figure 7 reveals dynamic effects for the reaction force in subplot a) in the form of relatively large oscillations, whereas the crack length history in subplot b) seems less affected. In the loading displacement interval of 4.0 to 5.0 mm, see subplot b), the leading and trailing edges move at approximately the same constant velocity of 158 m/s, and furthermore, the sliding displacement profile is also approximately constant. This will be elaborated below. The progression of the process zone length in this simulation is presented in Fig. 14. After substantial variation during early propagation, when large scale bridging conditions prevail, the zone length tends at the right of the figure towards an approximately constant value, as the small scale bridging limit is approached. Even then, the zone length is only approximately indicated by the analytical estimate of Eq. (1), $l_{SSB} = 41$ mm.

6.2 Sliding velocity in the process zone

The process zone sliding speed is a useful rate measure, since it describes the rate of the fracture processes (i.e., the rate at which through-thickness reinforcement such as z-pins or stitches are loaded, failed, and pulled out of the laminate). For steady-state crack propagation, namely propagation under conditions of time-invariance for the crack displacement profile in the process zone and crack velocity, the local sliding speed in the process zone is related to the crack displacement profile and crack tip speed through the following relationship:

$$\dot{\delta}_i(\xi) = \frac{\partial \delta_i}{\partial t} = - \frac{\partial \delta_i(\xi)}{\partial \xi} v_{tip} \quad (2)$$

where ξ is a longitudinal coordinate with origin at the crack tip, v_{tip} is the crack tip velocity and δ_i , for $i = 1$ or 2 , is the opening or sliding displacement (Fig. 15a).

Equation (2) defines the local sliding rate in all domains of steady-state crack growth as a function of the crack displacement profile and the crack tip speed, which are experimentally measurable quantities using a Digital Image Correlation (DIC) system. In addition, Eq. (2) can be used to verify if crack propagation is or can be approximated as steady-state in certain domains of crack growth in the numerical simulations. Figure 16 shows results for the specimens examined in Figs. 11 and 13 in the domains where steady-state conditions are suggested to hold at least approximately by the predicted crack tip speeds and crack profiles. The figure compares sliding velocities computed from simulations by (a) the right-hand side of Eq. (2), where the displacement profile $\delta(x)$ of the process zone at time t_n is differentiated with regard to the ξ -direction and multiplied by the crack tip speed, and (b) the difference in displacement between two time steps divided by the time step, i.e., $(\delta(\xi, t_n) - \delta(\xi, t_{n-1})) / (t_n - t_{n-1})$, where $t_n - t_{n-1}$ is the time step, equal to 1/200 of the total time domain. The sliding velocity profiles

computed by the two methods are presented for times corresponding to different applied displacements in the domains of presumed steady-state propagation.

The sliding speed profiles computed by the simulation and those estimated using Eq. (2) correlate well. The sliding speed varies within the process zone from a minimum at the leading edge to a maximum at the trailing edge. The horizontal solid lines in the figure show the average sliding speeds calculated over the process zone. The 20% of the process zone closest to the crack tip is excluded from the average, because the profile tends to be highly nonlinear there (see Fig. 15b). The near-tip domain is also difficult to measure accurately in an experiment and therefore is often a weak source of information.

The average sliding speed, $\dot{\delta}_{ave}$, estimated using Eq. (2) when crack growth is steady-state is given by:

$$\dot{\delta}_{ave} = \left\langle \frac{\partial \delta(\xi)}{\partial \xi} \right\rangle v_{tip} \quad (3a)$$

where $\langle \dots \rangle$ denotes an average over the relevant part of the process zone. The average sliding speed obtained from the exact numerical results of simulations will equal $\dot{\delta}_{ave}$ when crack growth is steady-state; in addition, should the crack profile be linear, the local sliding speed along the process zone will be uniform and equal to the average $\dot{\delta}_{ave}$ everywhere.

Another useful estimate of the average sliding rate within the process zone in steady state fracture is given by:

$$\dot{\delta}_{est} = \frac{\delta_c}{l_{pz}} v_{tip}, \quad (3b)$$

where l_{pz} is the process zone length, with $l_{pz} = l_{ssb}$ when the crack propagates in small scale bridging conditions. For small scale bridging and at moderate crack tip speeds the ratio $\frac{\delta_c}{l_{pz}}$ becomes independent of crack speed and is a function of the fracture energy G_b only (see Eq. 1). Figure 15b shows how $\dot{\delta}_{est}$ compares with $\dot{\delta}_{ave}$. The estimates of Eq. (3b) are shown in Fig. 16 with dashed lines. These estimates prove to be more stable in the regime of steady state growth than those obtained with Eq. (3a) (horizontal solid lines) since they depend on a global measure, l_{pz} , and not on the local details of the crack profile that are more affected by dynamic effects and numerical errors. The averaged quantities of Eqs. (3a) and (3b), when acceptably accurate, can be used to predict trends in behavior (see below).

For the specimen with no through-thickness reinforcement, the average sliding speeds in the selected time interval of Fig. 16 are $\dot{\delta}_{ave} = 6.4$ m/s and $\dot{\delta}_{est} = 6.0$ m/s and the average length of the process zone is 8.2 mm; for the specimen with through-thickness reinforcement, the average sliding speeds are $\dot{\delta}_{ave} =$

3.4 m/s $\dot{\delta}_{est} = 2.9$ m/s and the average length of the process zone 28 mm. Thus through-thickness reinforcement tends to slow down the crack and extend the fracture process zone.

Average sliding speeds and process zone lengths in the domains of steady-state propagation are presented for different loading speeds in Fig. 17. The results highlight that the average sliding speed across the process zone during steady-state propagation increases monotonically with the loading speed provided: (a) the length of the process zone remains similar for the different loading speeds, (b) multiple process zone formation is avoided and (c) the loading speed (and ramp time) is not so high (small) as to modify the response of the specimen (see Section 2). These conditions are satisfied in ENF specimens when the crack is propagating under approximate small scale bridging conditions for all loading speeds, as in the case of the specimen with no through-thickness reinforcement (Fig. 17b).

While the simplified domain is useful for designing experiments, the full solution space also contains quite complex behaviour. If the crack propagates under general large scale bridging conditions or when multiple process zones develop, the length of the process zone in the steady-state domains will vary significantly with loading speed, leading to corresponding variations in the response of the specimen. For example, the average sliding speed in the steady-state domains will decrease on increasing the loading speed (Fig 17a, specimen with through-thickness reinforcement). In addition, cases can be observed where steady-state propagation never occurs even if the crack is propagating under small scale bridging conditions, because the crack tip speed changes continuously during the fracture process; this typically occurs when the loading speeds are small and in the quasi-static case (see for instance Fig. 5). Conversely, cases can be observed when multiple domains of steady-state propagation with different sliding speeds are observed in a single simulation. These cases typically occur when the flexural oscillations of the specimen loaded dynamically cause propagation with alternating phases of crack arrest followed by phases of crack growth.

The results indicate that measurements of the loading speed are not enough to infer rate effects in an ENF specimen, because of the variety of different possibilities for the details of the fracture process for similar loading rates. Section 7 will show instead that the crack tip speed correlates with rates in the crack process zone and therefore experiments must attend to measuring the crack tip speed and preferably the crack profile as well. (In the flying wedge specimen (Sridhar et al., 2002), both the crack tip speed and the length of the process zone are directly related to the loading speed, because the load is applied directly to the fracture surfaces at locations that follow the crack motion. In such a case, steady-state crack propagation may occur both in small and large scale bridging, the problems above will not be present and the loading speed can be the reference parameter. However, the flying wedge is a special case for mode I loading only.)

7. Sensitivity to rate dependence in the cohesive law

The question of whether a particular dynamic test will yield data that contain information about possible rate dependence in the cohesive law can be addressed by analyzing the solutions presented in the previous sections as though they were the outcome of actual tests. Even this theoretical exercise is complex if undertaken most generally. Therefore a simplified approach is taken here by restricting the domains of the solutions considered to those where steady-state conditions hold at least approximately and assuming idealized cohesive laws. Considering a limited solution domain is conservative with respect to assessing information content, because the full domain must contain more information. Assuming idealized cohesive laws is also conservative, because even if a more general form of the law proves partly indeterminate when actual data are analyzed, the degrees of freedom that can be

determined in it cannot be less than those inferred for the simpler law. With the simplified approach, one can also work around the limitation of the ABAQUS code which was used in this study, that it cannot accept a general rate-dependent cohesive law.

Consider a separable linear cohesive law of the form

$$p_i = q_i + s_i \delta_i \quad (i = 1, 2; \delta_i \leq \delta_{ic}) \quad (4a)$$

$$p_i = 0 \quad (\delta_i > \delta_{ic}) \quad (4b)$$

which experiments have shown to be a useful approximation for stitches in tension (Turrettini, 1996) or shear (Massabò et al., 1998) and pins in tension or shear (Cartié et al., 2004) in cases of pure mode I or pure mode II loading. (The question of whether Eq. (4) is appropriate for cases of mixed mode loading is a topic to resolve in the future with actual data.) For negative values of s_i , the law defines the triangular laws used in the previous sections, which are good models of the intrinsic cohesive mechanisms of conventional tape laminates in the absence of through-thickness reinforcement.¹ Assume that rate dependence consists of linear changes in the parameters of Eq. (4):

$$q_i = q_i^{(0)} + \alpha_i \frac{\dot{\delta}_i}{c_i} \quad (i = 1 \text{ or } 2) \quad (5a)$$

$$s_i = s_i^{(0)} + \beta_i \frac{\dot{\delta}_i}{c_i} \quad (i = 1 \text{ or } 2) \quad (5b)$$

$$\delta_{ic} = \delta_{ic}^{(0)} + \gamma_i \frac{\dot{\delta}_i}{c_i} \quad (i = 1 \text{ or } 2) \quad (5c)$$

where $q_i^{(0)}$, $s_i^{(0)}$, and $\delta_{ic}^{(0)}$ are the parameter values for the static case, α_i , β_i and γ_i are dimensionless rate parameters, $\dot{\delta}_i = \partial \delta_i / \partial t$ is the local sliding rate and c_i is the longitudinal wave speed (Table 1).

The discussion of Section 6 reveals that the crack velocity and the crack profile are approximately invariant with some values v_{tip} and $\partial \delta_i(\xi) / \partial \xi$ for certain intervals during a delamination test, e.g., for load point displacements ranging from approximately 1 to 1.5 mm in the case of Fig. 11 or 4 to 5 mm in the case of Fig. 13. Tests of the sensitivity of an experiment to rate dependence are based here on analyzing the domains where the crack speed is uniform, v_{tip} , and the profile is uniform and approximately linear, so that its slope is well represented by the average slope, $\langle \partial \delta_i / \partial \xi \rangle$. According to Eq. (3a) the product of v_{tip} and the average slope $\langle \partial \delta_i / \partial \xi \rangle$ defines the average speeds, $\dot{\delta}_{i,ave}$, with $i=2$ (sliding) or $i=1$ (opening). In this regime, the capacity of an experiment for testing rate dependence is therefore indicated by the range of values of the product $\langle \partial \delta_i / \partial \xi \rangle v_{tip}$ that can be attained, e.g., by varying the load point velocity. The product $\langle \partial \delta_i / \partial \xi \rangle v_{tip}$ also remains a good indicator of the capacity

¹ When the cohesive law of Eq. (4) is used with cohesive interface elements, an initial linear elastic branch needs to be included as in Fig. 3 to control numerical difficulties. The opening or sliding displacement of Eq. (4) is then given by the difference of the total displacement across the crack and the displacement at the end of the linear branch.

of an experiment for testing rate dependence when the crack profile is not linear, as in the cases examined in Fig. 16, since its variations with crack tip speed gives an average measure of variations of the local sliding rates.

A number of simulations were executed with cohesive laws of the form of Eq. (4) with different values of the parameters q_i , s_i , and w_i that were representative of the range expected a conventional tape laminate. The linearly rising form of Fig. 3 was used for the load point displacement with various load point displacement rates, v_0 . In each simulation, a rate-independent cohesive law was specified, because a limitation of ABAQUS is that general rate-dependent laws are not permitted. However, in the domain where the crack profile is linear and the crack velocity is constant, a rate effect would simply imply different but fixed values of the parameters q_i , s_i , and w_i . By examining this domain for different cases, behavior for a rate-dependent variation such as Eq. (5) can be re-constructed; a simulation is executed, the domain of constant velocity and linear displacement profile is identified, and the quantity $\langle \partial \delta_i / \partial \xi \rangle v_{\text{tip}}$ is evaluated for this domain. The simulation is then taken to represent the law of Eqs. (3) and (4) for the value $\dot{\delta}_{i,ave} = - \langle \partial \delta_i / \partial \xi \rangle v_{\text{tip}}$.

To explore the procedure described above, simulations were performed on ENF specimens with $2L = 100$ mm, $h = 5$ mm and $a_0 = 20$ mm. The loading speeds were varied between 5 and 30 m/s with ramp times $t_0 = T_1 / 2$ or $t_0 = T_1$. A triangular cohesive law was used with maximum cohesive tractions and fracture energy varying in the following ranges: $\sigma_0 = 10 - 50$ MPa and $G_b = 0.25 - 2.5$ kJ/m². The small scale bridging length scales of Eq. (1), $l_{SSB} = \sqrt{\delta_c \bar{E} h / (4\sigma_0)}$, corresponding to the different laws are recorded in Table 3 along with the process zone lengths measured in the simulations in the phases of steady-state growth.

Domains of steady-state crack growth were identified by examining the curves of crack length versus applied displacement, e.g. Fig. 11, (which must be linear for steady-state conditions to be present), the speeds of the leading and trailing edge of the crack (which must be equal and constant) and the predictions of the average sliding speeds across the process zone obtained using the numerical results and Eq. (3) (the two predictions must be equal and constant in the domains of steady-state growth). Even in cases of steady-state propagation, large high frequency oscillations were observed in the crack tip speeds and the calculated average sliding speeds. These oscillations are a consequence of the dynamically applied load and the numerical discretization and their presence considerably complicates the identification of the steady-state domains. Steady-state domains were identified by the conditions that: the average values of the two crack tip speeds are similar; the average values of the two calculated average sliding speeds across the process zone are similar and the relative error between the two predictions falls below a limit value (selected as 10%). Only steady-state domains, where the process zone length l_{pz} would remain similar on varying the loading speed, have been considered. This assumption allows general conclusions to be drawn from results for different loading speeds.

The characteristics of identified steady-state domains are summarized in Figs. 18. Figure 18a shows the average sliding speeds in the steady-state domains obtained for different cohesive laws as a function of the loading speed. The average sliding speed generally increases with the loading speed, with the interesting variation that different domains of steady-state growth can occasionally be observed for the same value of the loading speed, e.g., for $\sigma_0 = 30$ MPa and $G_b = 0.5$ kJ/m² (they occur at different stages of crack growth). This is true also for $\sigma_0 = 30$ MPa and $G_b = 1.0$ kJ/m², where, however, for loading rates above 30 m/s the average crack sliding speed decreases.

Figure 18b shows the average sliding speeds in the steady-state domains as functions of the corresponding crack tip speeds for different cohesive laws. Points appear in pairs, plotted using the speeds of both the leading and the trailing edges of the crack. The closeness of the two points in any pair indicates the accuracy to which the steady state is attained. The corresponding process zone lengths l_{pz} are recorded in Table 3 along with the average crack tip speeds. The dashed curves in Fig. 18b are interpolating functions constrained to pass through the origin ($\dot{\delta}_{ave} = 0$, $v_{tip} = 0$). The monotonic trends of these curves is key to interpreting experiments: changing the crack tip speed causes significant and useful changes in the crack sliding speed, at least in the steady-state. In addition, the interpolating curves in Fig. 18b show a linear trend at moderate speeds that indicates that $\langle \partial \delta_i / \partial \xi \rangle$ is approximately constant on varying v_{tip} , Eq. (3), so that the cracks are propagating under small scale bridging conditions with an approximately constant size of the process zone length $l_{pz} = l_{ssb}$. Variations from the linear trend for larger speeds can be due to crack propagation conditions that differ from those of small scale bridging (typically leading to larger l_{pz}) or to changes in the small scale bridging crack profile due to high speeds (leading to shorter l_{pz}).

The results in this and the previous sections show that a significant range of crack sliding speeds can be generated in dynamic ENF tests for loading rates in the range of those that can be applied using a Kolsky bar system, encouraging the expectation that any rate dependence in the bridging constitutive behaviour can be determined.

Figure 19 shows average sliding speeds in the steady-state domains as functions of the crack tip speed for three cohesive laws characterized by different values of the maximum traction and the critical displacement and the same fracture energy $G_b = 0.5 \text{ kJ/m}^2$. The numerical results align nicely on a single curve, which is also well approximated by a straight line for crack tip speeds below $0.2 c_l$. This is expected because, in all cases studied, crack propagation in the steady-state domain does occur under conditions that are approximately small scale bridging, where the response should depend only on the area beneath the cohesive traction law, G_b , and not on its details. If, for example, the critical displacement is varied at fixed G_b , the ratio of the zone length to the critical crack displacement remains constant (see Eq. 1) so that the sliding speed estimate of Eq. (3b) remains constant. See also Table 3.

For small-scale bridging conditions, any material rate dependence that manifests itself in the cohesive fracture law should only affect the fracture energy G_b through changes in the average sliding speeds, $\dot{\delta}_{ave}$ or $\dot{\delta}_{est}$, (or the crack tip speed, v_{tip} , which is proportional to $\dot{\delta}_{ave}$ and $\dot{\delta}_{est}$ in steady-state propagation). The three rate parameters of Eq. (5) do not act independently; only their effect on the fracture energy (the area under the cohesive law) influences behaviour. In the case of linear rate dependence, this behavior can be described by the following relationship:

$$G_b = G_b^{(0)} \left(1 + \theta \frac{\dot{\delta}_{est}}{10^{-3} c_l} \right) \quad (6)$$

where $G_b^{(0)}$ is the quasi static value of G_b , $\dot{\delta}_{est}$ is the estimated average sliding speed in the process zone, Eq. 3b, and θ is a dimensional constant, whose value is kept near unity by the presence of the factor 10^3 .

Figure 20a presents again the numerical results of Fig. 18b through the estimated average sliding speed, $\dot{\delta}_{est}$ Eq. (3b), in the range of moderate crack tip speeds where the response can be approximated as linear. The dashed lines in the figure are linear interpolations of data corresponding to different cohesive laws, constrained to pass through the origin and, according to Eq. (3b), their slopes define the ratios δ_c/l_{ssb} , which give average measures of the process zone lengths of the different materials. For instance, the curve for $G_b = 0.5 \text{ kJ/m}^2$ has a slope $\delta_c/l_{ssb} = 0.0073$, so that $l_{ssb} = 4.56, 6.85$ and 13.7 mm for $\delta_c = 0.033, 0.05$ and 0.1 mm . These predictions of the small scale bridging length scale can be compared with the predictions of Eq. (1), shown in Table 3, to highlight again the influence of the non-uniform tractions acting along the crack when the crack propagates in the right hand part of the specimen: the numerical process zone length is approximately $0.53\sqrt{\delta_c \bar{E}h/(4\sigma_0)}$. The same ratio is observed for the other assumed cohesive laws in Fig. 20a.

The dashed lines in the diagram of Fig. 20b summarize the response of rate independent materials propagating in small scale bridging in the steady state regime through the function $\dot{\delta}_{est} = \frac{\delta_c}{l_{ssb}} v_{tip}$, with

$l_{ssb} = 0.53\sqrt{\delta_c \bar{E}h/(4\sigma_0)}$ and $G_b = G_b^{(0)} = 0.1 - 2.5 \text{ kJ/m}^2$. These curves can be used to construct steady-state behavior for a hypothetical rate-dependent material. For the examples shown, the rate dependent material is assumed to have the linear rate dependence of Eq. (6) and $G_b^{(0)} = 0.25 \text{ kJ/m}^2$. Each solid curve in the figure describes the response for an assumed value of the rate parameter θ ; the curve intersects the dashed curves corresponding to the different G_b at the average sliding speed $\dot{\delta}_{est}$ given by Eq. (6). The thick dashed curve with $\theta = 0$ define the response of a rate independent material with $G_b^{(0)} = 0.25 \text{ kJ/m}^2$.

For low crack tip speeds, the influence of rate effects on the average sliding speed is limited: when $v_{tip} < 50 \text{ m/s}$, variations in $\dot{\delta}_{est}$ due to rate effects remain below 10% even if the rate parameter θ is varied substantially from 0.0 to 10 ($\theta = 10$ for the material tested here gives $G_b = G_b^{(0)}(1 + 1.8\dot{\delta}_{est})$). The same is true for all $v_{tip} < 100 \text{ m/s}$ when θ remains below 5.0 (which corresponds to $G_b = G_b^{(0)}(1 + 0.9\dot{\delta}_{est})$). For higher crack tip speeds, rate dependence in the cohesive law can be readily observed in the numerical solutions (and therefore in experiments). For a crack tip speed of 400 m/s, for instance, the average sliding speed of 2 m/s of a rate independent material, increases to 2.5 m/s when $\theta = 1$ (and $G_b = 0.4 \text{ kJ/m}^2$) and to 3.5 m/s for $\theta = 3$ (and $G_b = 0.7 \text{ kJ/m}^2$). A rough guide for test design is inferred to be that the test should achieve crack velocities in excess of 100 m/sec. However, as observed in the numerical simulations performed above, only crack speeds below certain limit values are accessible in the tests since increasing the loading speed above certain values typically leads to multiple crack formation and other complicating mechanisms that might be advantageous for engineering performance but are unwelcome in tests intended to calibrate rate dependence. The limit values depend on the geometry of the specimen and the elastic and inelastic properties of the material.

Maps similar to that shown in Fig. 20b can be constructed for different values of the quasi-static fracture energy $G_b^{(0)}$. In the maps the dashed line corresponding to a rate independent material with $G_b = G_b^{(0)}$ will define the lower envelope of the curves for the hypothetical rate dependent material. The behavioral maps can be used to interpret experimental results in domains of steady state growth in ENF specimens. The main limitations in the use of the maps are due to the assumption of small scale bridging crack growth that has been used to construct them. This limitation is removed when dealing with fracture tests where the length of the process zone during dynamic crack growth is directly related to the loading speed, the geometry of the specimen and the cohesive parameters. An example of such a specimen is the flying wedge specimen for mode I fracture analysis (Sridhar et al., 2002). In the flying wedge specimen, after a transient phase, crack propagation occurs under steady-state conditions, considerably simplifying the analysis of the problem (Massabò et al., in preparation).

8. Conclusions

A numerical investigation has been presented aimed at designing a test geometry and a loading procedure to infer mode II dynamic cohesive laws for through-thickness reinforced laminates from dynamic End Notched Flexural tests. The design of the test geometry was concerned with the size of the specimen (length and thickness) and the length of the initial notch; the design of the displacement controlled loading procedure including the loading speed and the time to ramp the loading speed from zero to the required value. Idealized rate-independent cohesive laws with parameters chosen to represent either through-thickness reinforcement, such as z-pins, or unreinforced laminates were used in simulations. Behavior expected for rate-dependent cohesive laws was inferred from limiting solutions.

The analyses show the existence of regimes, within the full computed solution space, where crack growth is approximately steady-state. A simplified approach to inferring rate effects in the cohesive law can then be taken by restricting the domains of the solutions considered to the steady state domains. Considering a limited solution domain is conservative with respect to assessing information content, because the full domain must contain more information.

In the steady state regimes, the local sliding speed in the process zone, which is the parameter that controls rate effects in the cohesive law, is a known function of the crack tip speed and the sliding displacement profile. Both of these quantities could be measured using a digital image correlation system. In addition, the average sliding speed along the process zone when the crack is propagating in steady-state conditions coincides with the local sliding speed if the profile is approximately linear. In this case numerical solutions obtained for a rate-independent cohesive law would represent general rate-dependent materials since a rate effect would simply imply different but fixed values of the cohesive parameters.

By examining the steady state domains for different rate independent cases, behavior for assumed rate-dependent variations can be re-constructed. In the ENF specimen this can be done if the crack is propagating in small scale bridging conditions; in other specimens where the load is applied directly onto the crack surfaces, such as the mode I flying wedge specimen, behavior of rate-dependent materials can also be reconstructed for general large scale bridging conditions using solutions for rate-independent materials.

The design of the test procedure was based on the requirements listed in the Introduction, for which the following conclusions are reached.

- Generate dynamic crack propagation in the range of speeds where the action of through-thickness reinforcement will be relevant. This requirement indicates that large crack speeds should be avoided, namely when the crack tip speed should be lower than 20-30% the longitudinal wave speed, $v_{tip} < 0.2 - 0.3c_l$; for large crack speeds the fracture process is dominated by the kinetic energy and the effects of the reinforcement on the solution become negligible. The analyses performed show that very large crack tip speeds are not easily obtained in ENF tests since increasing the loading speed above a certain limit induces other unwelcome mechanisms that prevent the crack tip from reaching very high speeds, such as the formation of multiple delaminations (the same effect is observed by decreasing the loading ramp time). Ramp times on the order of the first period of vibration of the specimen, $t_0 = 0.5 - 1 T_1$, and loading speeds in the range of those that can be applied using a Kolsky bar system, $v_0 = 5 - 40$ m/s, satisfy this requirement.
- Generate dynamic crack propagation in the range of speeds where rate effects in the cohesive parameters will be measurable. The analyses show that rate effects in the cohesive laws are expected to be measurable in the experimental tests since significant and useful changes in the average sliding speeds can be obtained by varying the loading speeds in the range applicable using a Kolsky bar. In addition, very low crack speeds should be avoided since rate effects will not be easily measurable there; for instance, for crack propagation in the small scale bridging limit and the linear rate dependence assumed in Eq. (6), the crack tip speeds should be $v_{tip} > 0.02c_l$ (Fig. 20b).
- Generate crack propagation in the domain where the process zone is developing and also where it is fully developed, thus maximizing the information content pertaining to all model parameters; crack propagation should be stable an initial domain of growth to facilitate the derivation of the parameters. To satisfy this requirement the half-length of the ENF specimen should be several times longer than the small scale bridging characteristic length scale, which is a function of the square root of the thickness of the specimen; and the length of the notch should be kept long enough. While this requirement can be satisfied in conventional tape laminates, where l_{ssb} remains in the range 5-20 mm, using sufficiently long specimens in through-thickness reinforced laminates, where $l_{ssb} = 40-60$ mm (in the examples shown) would lead to very long and much too compliant specimens.
- When the crack is propagating in the second half of the specimen, the stress field is not uniform along the crack surfaces and differs from that for which the characteristic length scales of the problem were derived; in addition, friction along the crack surfaces below the loading point would affect the results and should be properly modelled.
- Avoid the formation of multiple cracks in the specimen. The initiation and propagation of cohesive cracks in locations other than the initial notch is controlled by the geometry of the specimen and the loading procedure. The mechanisms can be avoided using longer specimens, increasing the ramp time and reducing the loading speed. In addition, the shape of the cohesive law has an important effect on this mechanism: multiple cracks are more likely when the bridging tractions are an increasing function of the relative crack displacement.
- Avoid failure by mechanisms other than delamination fracture, namely compressive or tensile failure at the midspan. To satisfy this requirement shorter and thicker specimens should be used.

- Avoid large flexural oscillations of the specimen as well as the development of high order, high frequency waves in the desired range of crack speeds. This requirement leads to the same limitations on ramp times and loading speeds listed above and limits the compliance of the specimen, whose dimensions were set equal to $2L = 100$ mm and $2h = 10$ mm.

Acknowledgments: RM supported by the U.S. Office of Naval Research through contract no. N00014-05-1-0098, administered by Dr. Yapa D.S. Rajapakse. BNC, CLL and RM supported by the U.S. Army Research Office through contract number DAAD19-99-C-0042, administered by Dr. David Stepp. The authors thank Dr. A. Cavicchi who performed some of the ABAQUS simulations.

References

- Andrews, M.G., Massabò, R., Cavicchi, A., B.N. Cox (2009), Dynamic interaction effects of multiple delaminations in plates subject to cylindrical bending, *Int. Journal of Solids and Structures*, 46, 1815-1833.
- Aveston, J., Cooper, G.A., and Kelly, A., Single and Multiple Fracture, The Properties of Fiber Composites, IPC Science and Technology Press Ltd., Guildford, Surrey, National Physical Laboratory, London 1971, pp. 15-24.
- Bao, G., and Suo, Z., 1992. Remarks on crack-bridging concepts. *Applied Mechanics Review* 24, 355-366.
- Brandinelli, L., Massabò, R., (2003), Free vibrations of delaminated beam-type structures with crack bridging, *Composite Structures*, 61, 129-142.
- Brandinelli, L., and Massabò, R., 2004. Mode II weight functions for delamination problems. *International Journal of Fracture* in preparation.
- Cartié, D.R., Cox, B.N., and Fleck, N.A., 2004. Mechanisms of crack bridging by composite and metallic rods. *Composites A35*, 1325-1336.
- Camanho, P., Davila, C., De Moura, M. (2003), Numerical simulation of mixed mode progressive delamination in composite materials, *Journal of Composite Materials* 37, 1415-1438.
- Chang, P., Mouritz, A.P., and Cox, B.N., 2006. Properties and failure mechanisms of Z-pinned laminates in monotonic and cyclic tension. *Composites, Part A* 37, 1501-1513.
- Chang, P., Mouritz, A.P., and Cox, B.N., 2008. Elevated temperature properties of pinned composite lap joints. *Journal of Composite Materials* 42, 741-769.
- Cox, B.N., 2005. Snubbing effects in the pullout of a fibrous rod from a laminate. *Mechanics of Advanced Materials and Structures* 12, 85-98.
- Cox, B.N., and Sridhar, N., 2002. A traction law for inclined fibre tows bridging mixed mode cracks. *Mechanics of Composite Materials and Structures* 9, 299-331.
- Cox, B.N., Massabò, R., and Kedward, K.T., 1996. Suppression of delaminations in curved structures by stitching. *Composites Part A* 27A, 1133-1138.
- Cox, B.N., Sridhar, N., and Beyerlein, I., 2001. Inertial Effects in the Pullout Mechanism During Dynamic Loading of a Bridged Crack. *Acta Materialia* 49, 3863-77.

- Dransfield, K., Baillie, C., and Mai, Y.-W., 1994. Improving the delamination resistance of CFRP by stitching - a review. *Composites Science and Technology* 50, 305-317.
- Dransfield, K., Jain, L.K., and Mai, Y.-W., 1998. On the effects of stitching in CFRPs-I. Mode I delamination toughness. *Composites Science and Technology* 58, 815-827.
- Freund, L.B., *Dynamic fracture mechanics*, Cambridge University Press, UK.
- Glaessgen, E.H., Raju, I.S., and Poe, C.C., 1999. Delamination and Stitch failure in stitched composite joints. AIAA Journal paper 1247.
- Holt, D.J., 1982. Future Composite Aircraft Structures May be Sewn Together. *Automotive Engineering* 90.
- Jain, L.K., and Mai, Y.-W., 1995. Determination of mode II delamination toughness of stitched laminated composites. *Composites Science and Technology* 55, 241-253.
- Jain, L.K., Dransfield, K., and Mai, Y.-W., 1998. On the effects of stitching in CFRPs-II. Mode II delamination toughness. *Composites Science and Technology* 58, 829-837.
- Lee, C., and Liu, D., 1990. Tensile strength of stitching joint in woven glass fabrics. *Journal of Engineering Materials and Technology* 112, 125-130.
- Liu, H.-Y., Yan, W., Yu, X.-Y., and Mai, Y.-W., 2007. Experimental study on effect of loading rate on mode I delamination of z-pin reinforced laminates. *Composites Science and Technology* 67, 1294-1301.
- Massabò, R., and Cox, B.N., 1999. Concepts for bridged mode II delamination cracks. *Journal of the Mechanics and Physics of Solids* 47, 1265-1300.
- Massabò, R., Mumm, D.R., and Cox, B.N., 1998. Characterizing mode II delamination cracks in stitched composites. *International Journal of Fracture* 92, 1-38.
- Mouritz, A.P., and Cox, B.N., 2000. A mechanistic approach to the properties of stitched laminates. *Composites A* 31, 1-27.
- Rhodes, M.D., and Williams, J.G., Concepts for Improving Damage Tolerance of Composite Compression Panels, 5th DoD/NASA Conference on Fibrous Composites in Structural Design, 1981.
- Rugg, K.L., Cox, B.N., Ward, K., and Sherrick, G.O., 1998. Damage mechanisms for angled through-thickness rod reinforcement in carbon-epoxy laminates. *Composites Part A* 29A, 1603-1613.
- Sawyer, J.W., 1985. Effect of stitching on the strength of bonded composite single lap joints. *AIAA Journal* 23, 1744-1748.
- Smith, E., (1989) The size of the fully developed softening zone associated with a crack in a strain-softening material- I. A semi-infinite crack in a remotely loaded infinite solid. *Int. J. Engng. Sci.*, **27**, 301-307.
- Soden, P., Hinton, M. and Kaddour, A. (2002), Biaxial test results for strength and deformation of a range of E-glass and carbon fibre reinforced composite laminates: failure exercise benchmark data, *Composites Science and Technology* 62, 1489-1514.
- Song, B., and Chen, W., 2004. Loading and unloading split Hopkinson pressure bar pulse-shaping techniques for dynamic hysteretic loops. *Experimental Mechanics* 44, 622-627.

- Sridhar, N., Massabò, R., Cox, B.N., and Beyerlein, I., (2002) Delamination dynamics in through-thickness reinforced laminates with application to DCB specimen, *Int. Journal of Fracture*, 118, 119-144.
- Sridhar, N., Yang, Q.D., and Cox, B.N., 2003. Slip, Stick and Reverse Slip Characteristics during Dynamic Fiber Pullout. *Journal of the Mechanics and Physics of Solids* 51, 1215-1241.
- Sun, X., Tong, L., Wood, M.D.K., and Mai, Y.-W., 2004. Effect of stitch distribution on mode I delamination toughness of laminated DCB specimens. *Composites Science and Technology* 64, 967-981.
- Suo, Z., Bao, G., and Fan, B. (1992), Delamination \mathcal{R} -Curve phenomena due to damage, *J. Mech. Phys. Solids*, **40**, 1-16.
- Tada, Y., and Ishikawa, T., 1989. Experimental evaluation of the effects of stitching on CFRP laminate specimens with various shapes and loadings. *Key Engineering Materials* 37, 305-316.
- Tong, L., Cleaves, K., Kruckenburg, T., and Stevens, G.P., 1998a. Strength of RTM single lap joints with transverse stitching. *Key Engineering Materials* 137, 195-202.
- Tong, L., Jain, L.K., Leong, K.H., Kelly, D., and Herszberg, I., 1998b. Failure of transversely stitched RTM lap joints. *Composites Science and Technology* 58, 221-227.
- Turrettini, A., (1996) An Investigation of the Mode I and Mode II Stitch Bridging Laws in Stitched Polymer Composites. Masters Thesis, Department of Mechanical and Environmental Engineering, University of California, Santa Barbara.

TABLES

Table 1. Material properties for quasi-isotropic carbon/epoxy laminate related to coordinate system in Figure 1. The ultimate stresses σ_u in tension and compression are obtained from experiments presented in Soden et al. (2002).

E_z, E_x	50 GPa
E_y	10 GPa
$\nu_{zy}, \nu_{xy}, \nu_{zx}$	0.28
G_{zy}, G_{xy}	5 GPa
G_{zx}	$E_z / 2(1 + \nu_{zx})$
ρ (mass density)	1600 kg/m ³
$c_l = \sqrt{\frac{E_z}{\rho}}$	5590 m/s
σ_u (tension)	750 MPa
σ_u (compression)	630 MPa

Table 2: Parameters defining the three cohesive laws used in most simulations.

	σ_0 [MPa]	δ_c [mm]	G_b [kJ/m ²]
Not reinforced (triangular)	20	0.05	0.5
Reinforced (triangular)	20	0.5	5.0
Reinforced (trapezoidal)	10	0.5	5.0

Table 3 - Small scale bridging length scale, $l_{SSB} = \sqrt{\delta_c \bar{E} h / (4\sigma_0)}$, Eq. (1), for triangular cohesive laws with the parameter values used in the numerical simulations of Fig. 18; numerical process zone lengths and crack tip speeds in the approximate steady-state domains of Fig. 18.

	l_{SSB} (mm) (Eq. 1)	l_{pz} , process zone length - simulations (mm)				
		$v_0 = 5$ m/s	$v_0 = 10$ m/s	$v_0 = 20$ m/s	$v_0 = 30$ m/s	others (m/s)
$G_b = 0.25 \text{ kJ/m}^2$, $\sigma_0 = 20 \text{ MPa}$	9.2	4.9 ($v_{tip}=226$)	4.85 ($v_{tip}=352$) 5.0 ($v_{tip}=459$)	5.1 ($v_{tip}=1016$)	5.3 ($v_{tip}=838$)	5.4 ($v_0 = 15$) ($v_{tip}=876$)
$G_b = 0.5 \text{ kJ/m}^2$, $\sigma_0 = 20 \text{ MPa}$	13	8.7	7.1	8.2	-	-
$G_b = 0.5 \text{ kJ/m}^2$, $\sigma_0 = 30 \text{ MPa}$	8.7	4.7 ($v_{tip}=138$)	4.15 ($v_{tip}=414$)	4.5 ($v_{tip}=903$) 4.7 ($v_{tip}=1118$) 4.9 ($v_{tip}=1437$)	-	-
$G_b = 0.5 \text{ kJ/m}^2$, $\sigma_0 = 10 \text{ MPa}$	26	-	16.5	10.	-	-
$G_b = 0.75 \text{ kJ/m}^2$, $\sigma_0 = 30 \text{ MPa}$	10.6	6.3 ($v_{tip}=140$)	5.5 ($v_{tip}=256$) 5.8 ($v_{tip}=345$)	5.7 ($v_{tip}=703$)	5.0 ($v_{tip}=1300$)	-
$G_b = 1.0 \text{ kJ/m}^2$, $\sigma_0 = 30 \text{ MPa}$	12.3	-	7.1 ($v_{tip}=193$)	-	7.9 ($v_{tip}=1015$)	6.5 ($v_0 = 40$) ($v_{tip}=348$)
$G_b = 2.5 \text{ kJ/m}^2$, $\sigma_0 = 50 \text{ MPa}$	11.6	-	7.5 ($v_{tip}=52$)	5.7 ($v_{tip}=351$) 6.3 ($v_{tip}=580$)	8.15 ($v_{tip}=1015$)	-

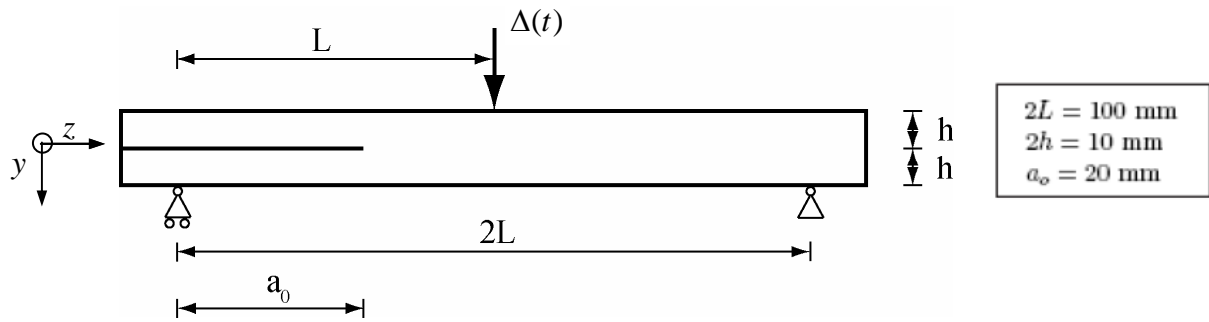


Figure 1: Dimensions of End Notched Flexural specimen (ENF) and reference system.

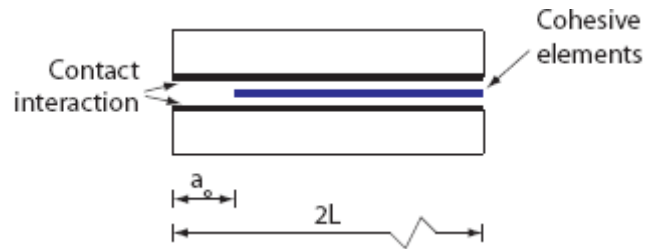


Figure 2: Exploded schematic illustration of an ENF specimen in the finite element model. Zero-thickness cohesive elements constitute the bonding between the beams, and contact interaction prevents interpenetration.

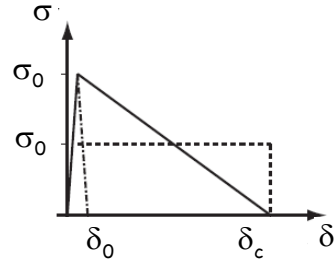


Figure 3: Trapezoidal and triangular cohesive laws used in the simulations.

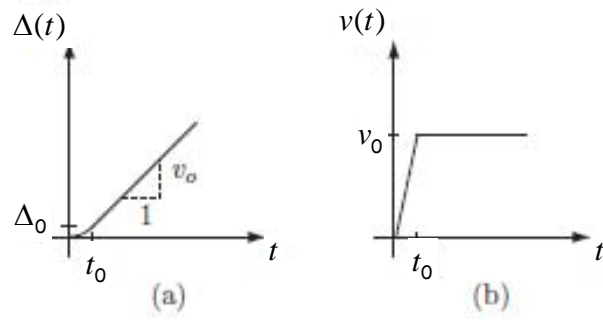


Figure 4: Schematic displacement (a) and velocity (b) histories for the load point in the simulations.

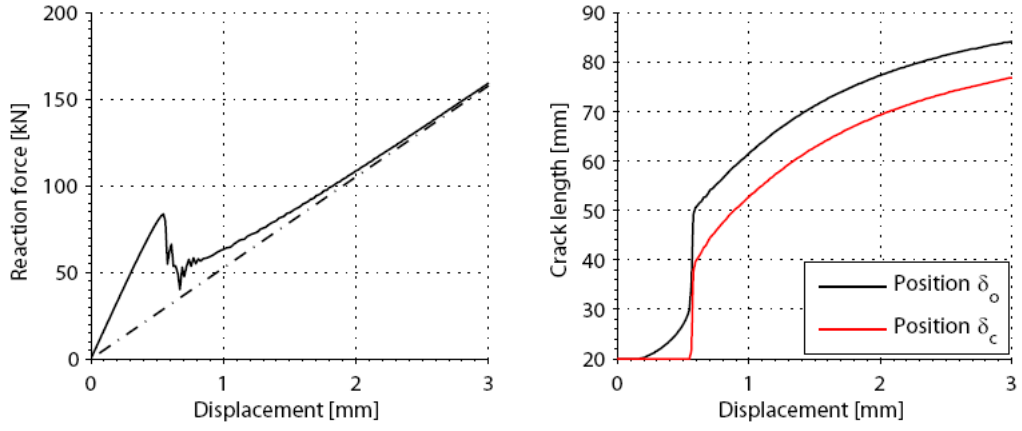


Figure 5: Results for quasi-statically loaded ENF specimen with $2L = 100$ mm and cohesive law corresponding to triangular with no reinforcements ($\delta_c = 0.05$ mm and $G_b = 0.5$ kJ/m²). In both sub-plots the horizontal axis represents the load point displacement, see Figure 1. The sub-figures are a) reaction force at loading point, and b) position of leading (black line) and trailing (red line) edge of the process zone. The dashed line in subplot b) is the load-displacement curve of a completely damaged specimen (two beams each of thickness h) calculated from shear deformable beam theory.

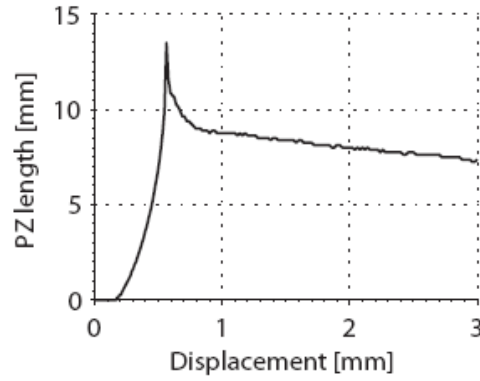


Figure 6: Process zone length, i.e. the vertical distance between the black and red lines in Figure 5b, as a function of loading displacement (small scale bridging length $l_{SSB} = 13$ mm, Eq. 1).

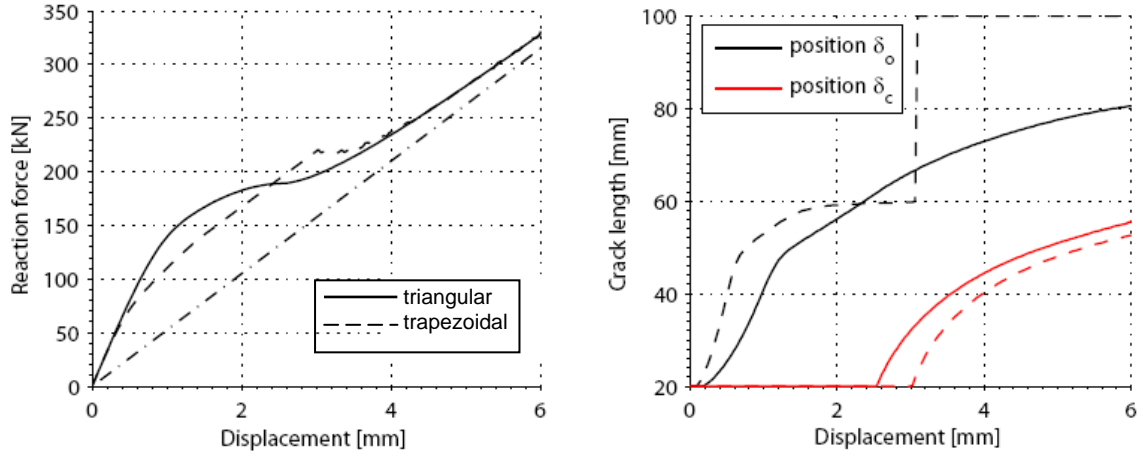


Figure 7: Results for a mode II ENF specimen loaded under quasi-static conditions with $2L = 100$ mm, $a_0 = 20$ mm and $G_b = 5.0$ kJ/m². Cohesive laws correspond to fracture properties with reinforcements where the solid line represents the triangle-shaped and the dashed is the trapezoidal.

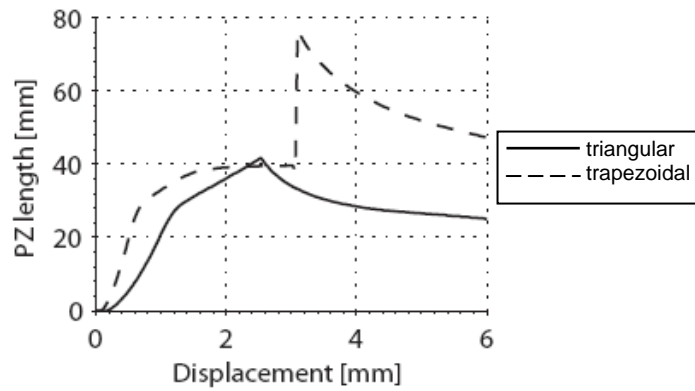
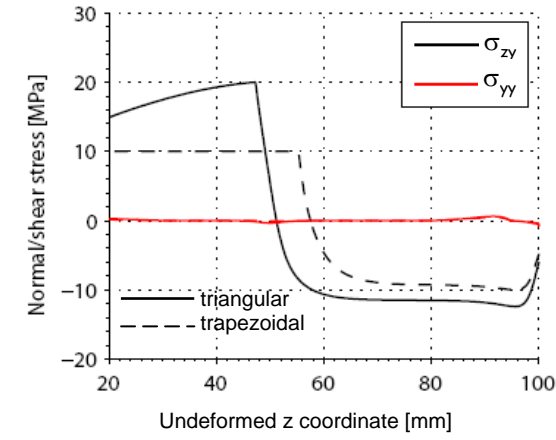
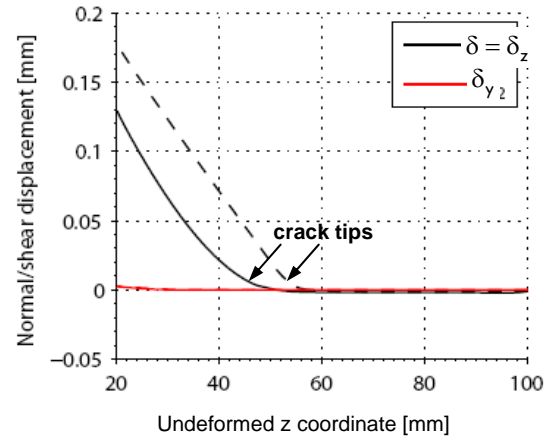


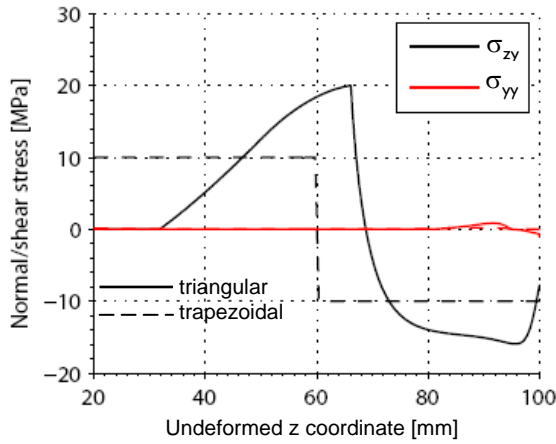
Figure 8: Process zone length corresponding to results described in Figure 7 (small scale bridging lengths: $l_{SSB} = 41$ mm (triangular) and $l_{SSB} = 58$ mm (trapezoidal)).



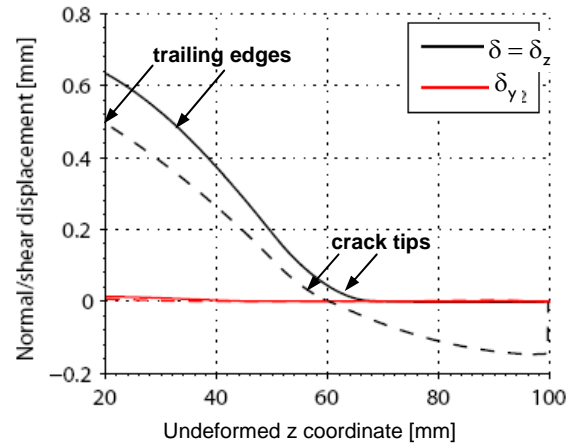
(a)



(b)



(c)



(d)

Figure 9: (a) and (b) Stresses (σ_{zy} , shear, and σ_{yy} , normal) and relative displacements (δ_z , sliding, and δ_y , opening) along the cohesive elements at an applied displacement of 1.2 mm in the simulation presented in Fig. 7. The pre-notch tip is located at $z = 20$ mm. The solid line represents the triangular cohesive law and dashed the trapezoidal. (c) and (d) solutions at an applied displacement of 3 mm.

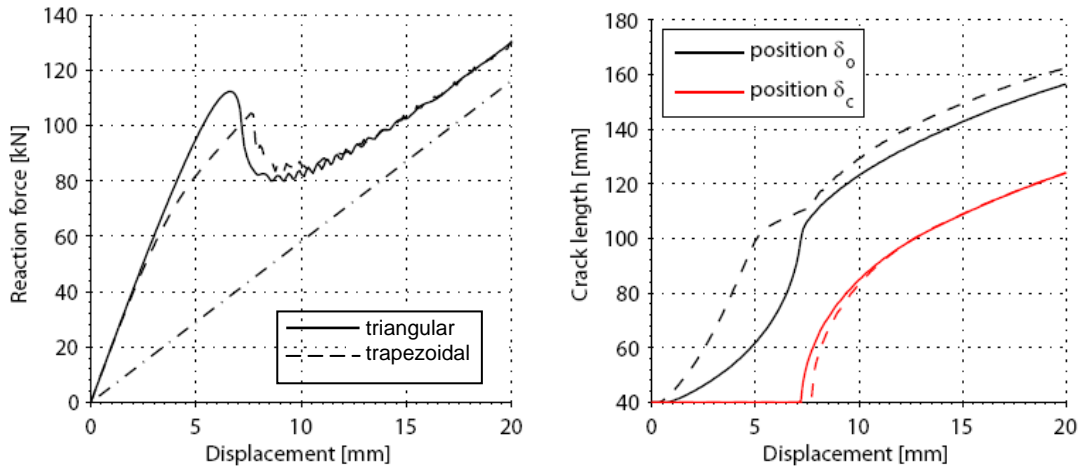


Figure 10: Quasi-static results for large specimen, $2L = 210$ mm, $a_0 = 40$ mm and $G_b = 5.0$ kJ/m². Cohesive laws correspond to fracture properties with reinforcements, the solid line is triangular and the dashed is trapezoidal.

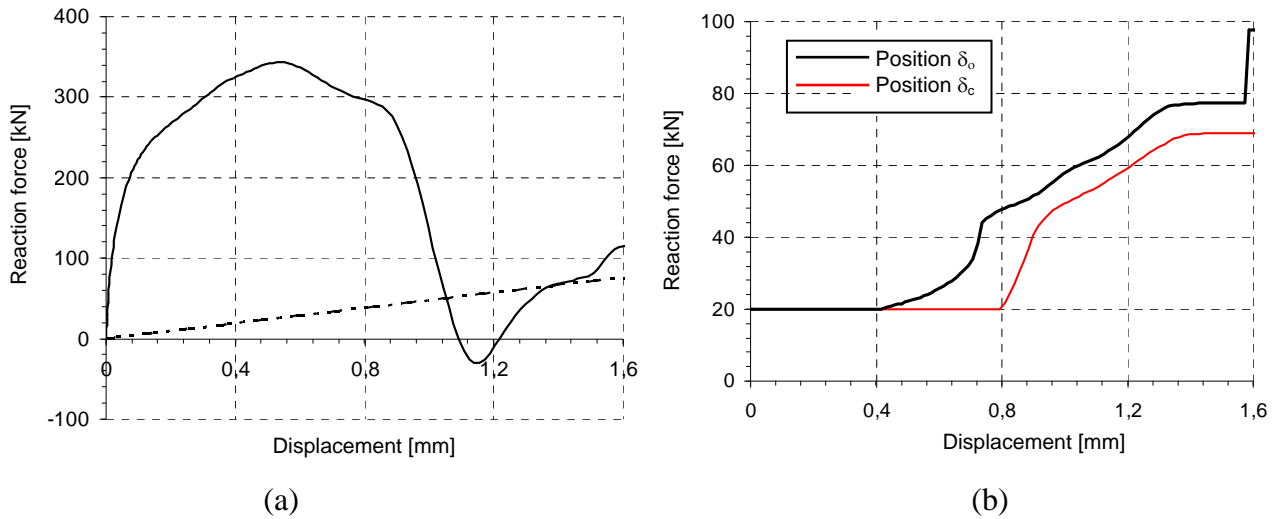


Figure 11: Results for specimen with $2L = 100$ mm, $a_0 = 20$ mm, $v = 20$ m/s and $t_0 = T_1/2$. Cohesive law is triangular corresponding to no reinforcement ($\delta_c = 0.05$ mm). In both sub-plots the horizontal axis represents the load point displacement. The sub-figures are a) reaction force at loading point, and b) position of leading and trailing edge of the process zone.

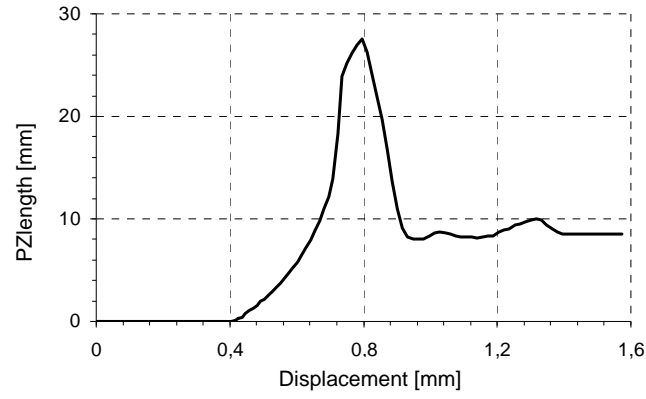


Figure 12: Process zone length, i.e. the vertical distance between the black and red lines in Figure 11, as a function of loading displacement (small scale bridging length $l_{SSB} = 13$. mm).

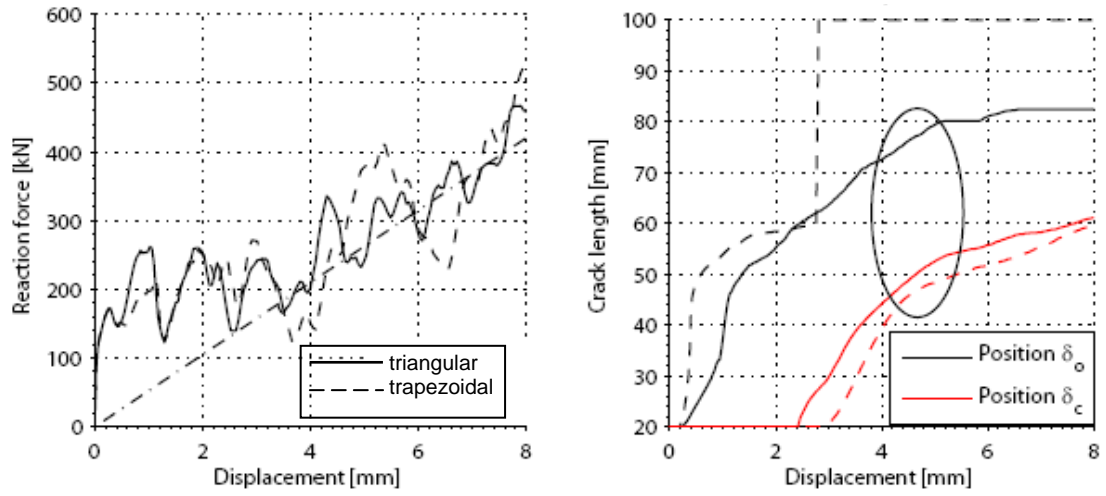


Figure 13: Results for specimen with $2L = 100$ mm, $a_0 = 20$ mm, $v = 20$ m/s and $t_0 = T_1$. Cohesive laws correspond to a z-pinned laminate, the solid line is triangular and the dashed is trapezoidal.

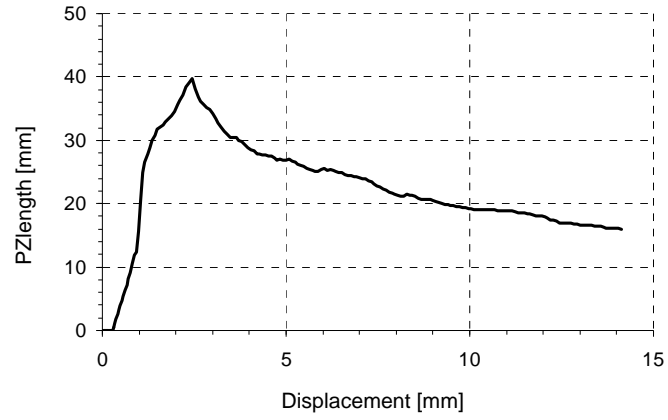
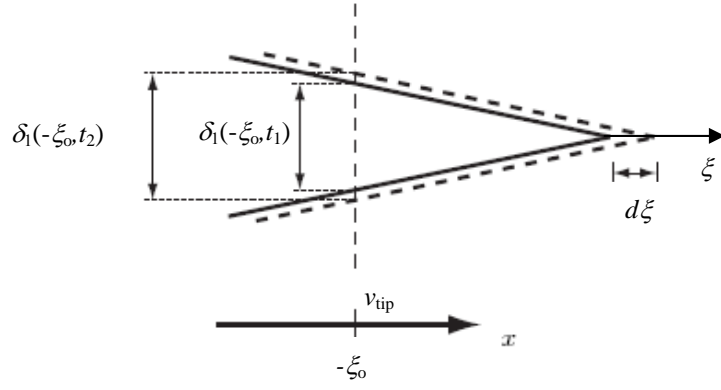
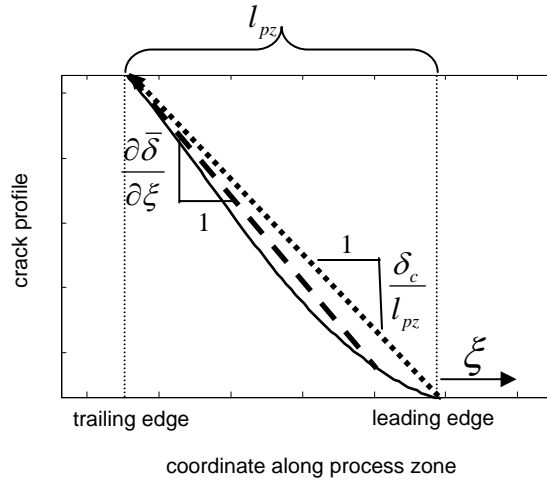


Figure 14: Process zone length, i.e. the vertical distance between the black and red lines in Figure 13, as a function of loading displacement (small scale bridging length after Eq. (1), $l_{SSB} = 41$ mm).



(a)



(b)

Figure 15: (a) Schematic illustration of opening profile for a pure mode I crack. (b) Exemplary sliding profile in the process zone: numerical solution (solid line), average profile along relevant portion of the process zone (dashed line), estimate of average profile obtained joining leading and trailing edges (dotted line).

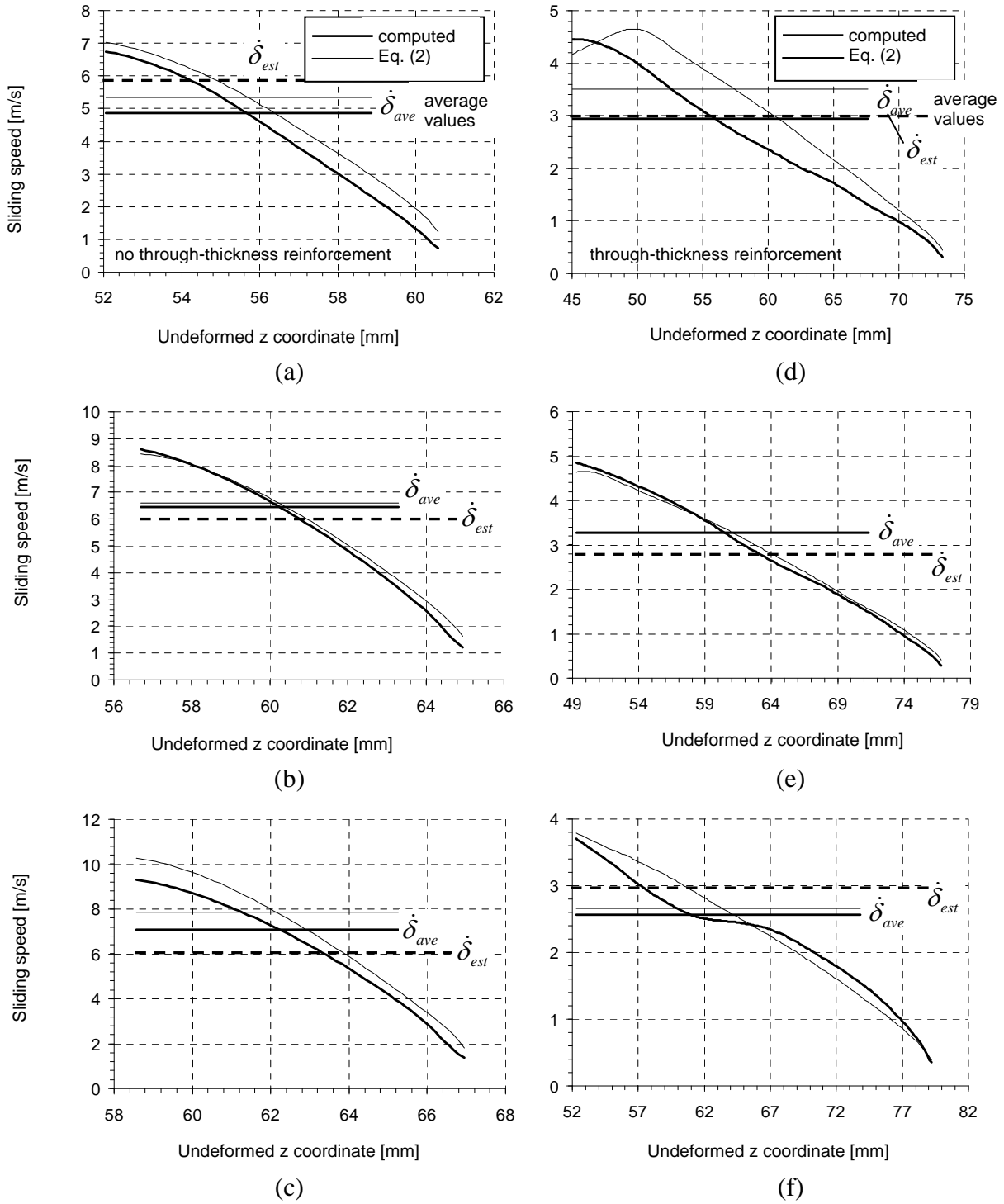


Figure 16: Actual relative sliding speeds in the process zone (from direct numerical calculations) and those predicted by Eq. (2). The simulations corresponds to results in Figures 11 (diagrams a-c) and 13 (diagrams d-f), at load point displacements of 1.06, 1.15, 1.19 mm (subplots a-c) and 4.1, 4.6 and 4.9 mm (subplots d-f). The horizontal solid lines define average sliding speeds calculated over the relevant part of the process zone; the horizontal dashed line defines average estimate as given in Eq. (3b).

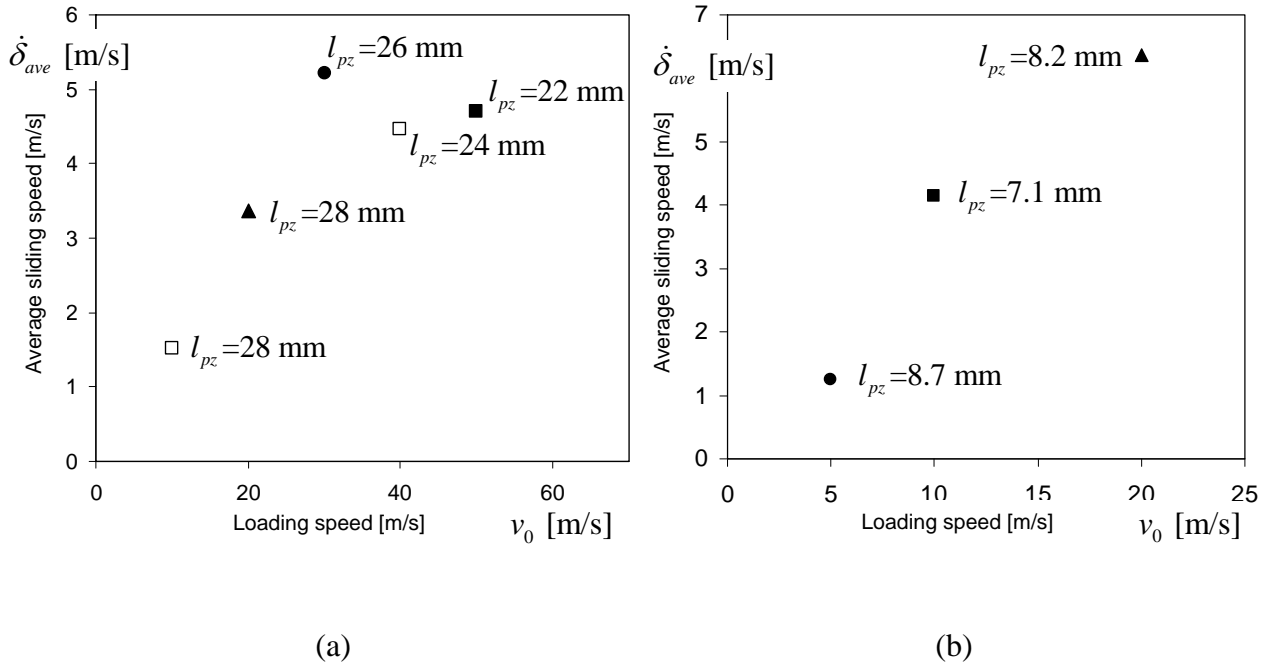
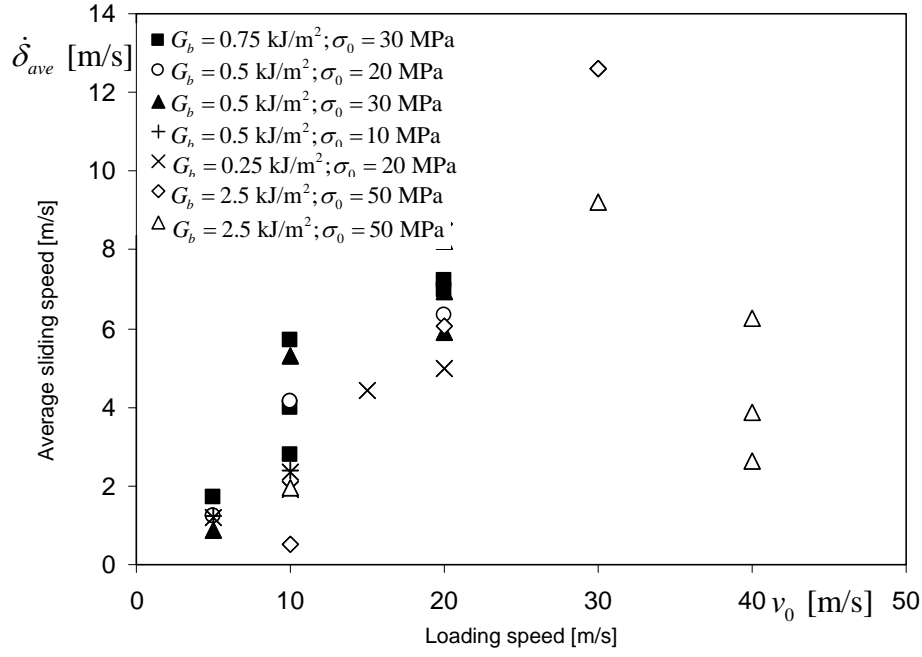
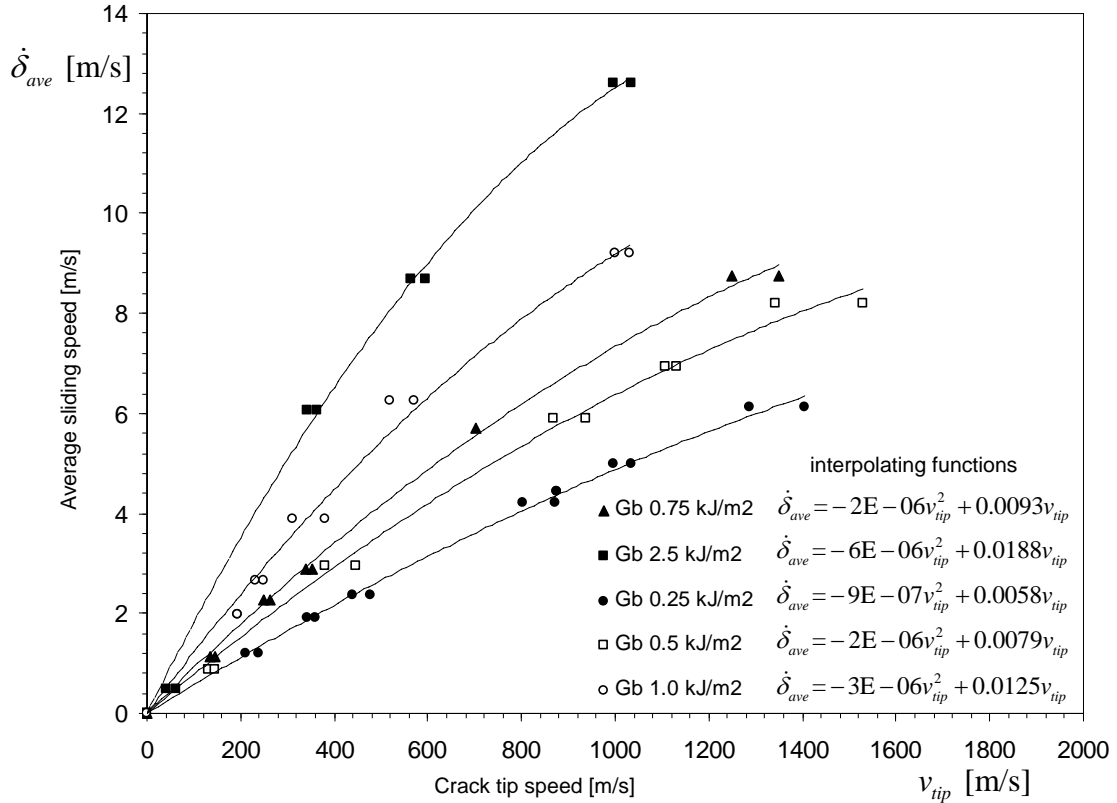


Figure 17. Average sliding speeds in the process zones in domains of steady-state crack propagation in (a) specimens with through-thickness reinforcement with $G_b = 5.0 \text{ kJ/m}^2$ (small scale bridging length of Eq. (1), $l_{SSB} = 41 \text{ mm}$). (b) specimens with no through-thickness reinforcement with $G_b = 0.5 \text{ kJ/m}^2$ (small scale bridging length of Eq. (1), $l_{SSB} = 13 \text{ mm}$).



(a)



(b)

Figure 18. Average sliding speeds in the process zones in domains of steady-state crack propagation and small scale bridging as functions of (a) the loading speed and (b) the crack tip speed for different triangular cohesive laws. The smooth dashed curves in (b) are interpolating functions used to construct plots of anticipated trends for hypothetical rate-dependent materials.

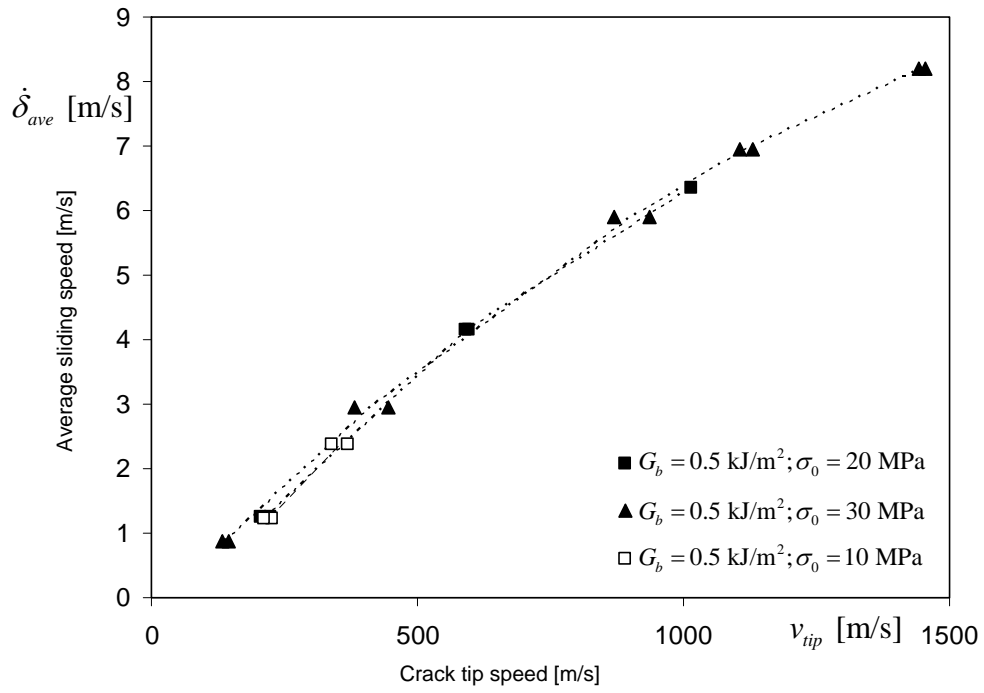


Figure 19. Average sliding speeds in the process zones in domains of steady-state crack propagation and small scale bridging as functions of the crack tip speed for three triangular cohesive laws with fracture energy $G_b = 0.5 \text{ kJ/m}^2$.

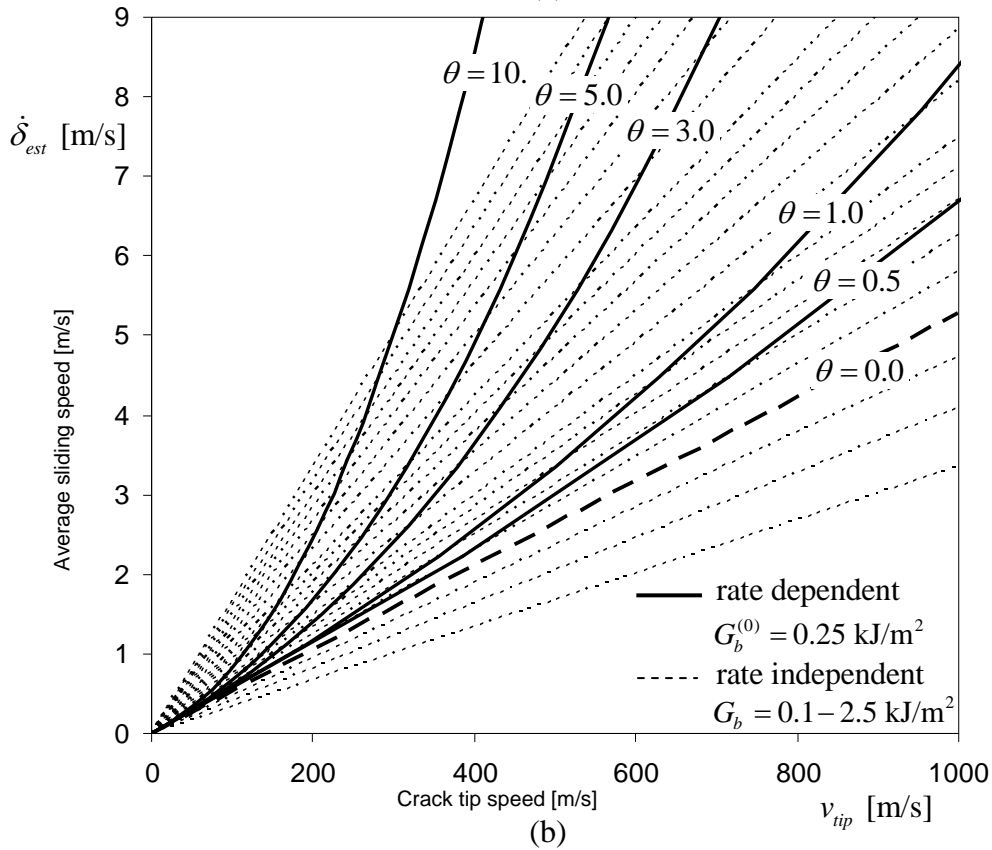
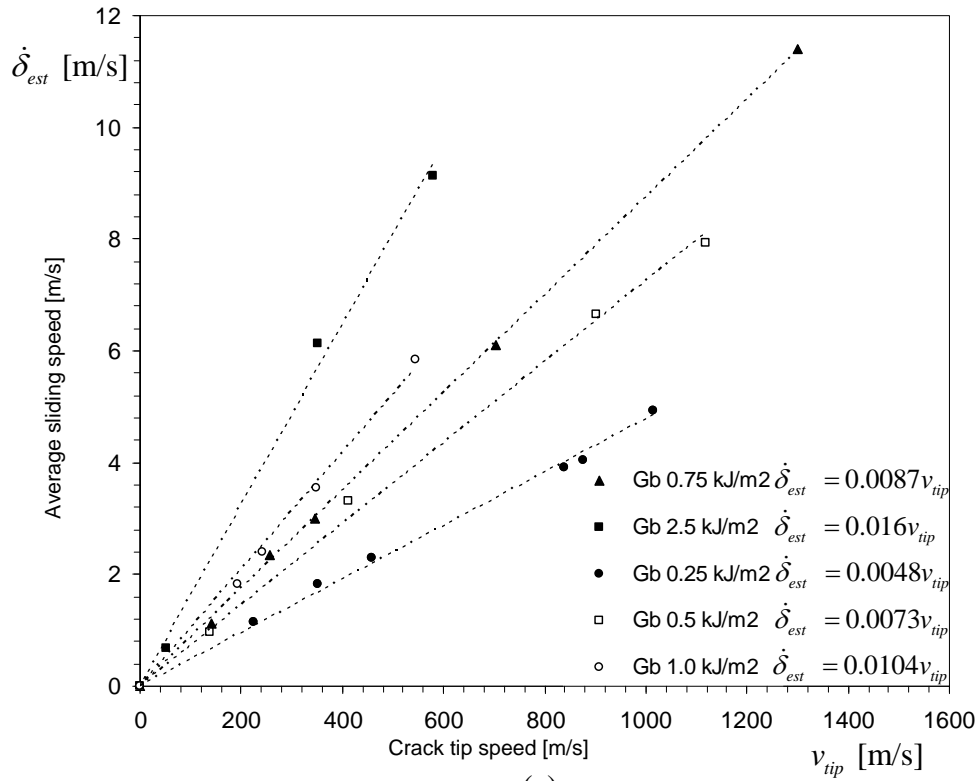


Figure 20. (a) Average sliding speeds predicted within the process zones in domains of steady-state crack propagation as functions of the crack tip speeds; the dashed lines are interpolating functions. (b) Average sliding speeds predicted within the process zones in domains of steady-state crack propagation and small scale bridging as functions of the crack tip speeds for rate independent materials, Eq. (3b) and hypothetical rate-dependent materials (solid curves) with quasi static fracture energy $G_b^{(0)} = 0.25 \text{ kJ/m}^2$ and rate dependence given by Eq. (6).